Theory of nonaxisymmetric vertical displacement events in tokamaks

2011 Nucl. Fusion 51 053007

(http://iopscience.iop.org/0029-5515/51/5/053007)

IOP Publishing and International Atomic Energy Agency Nuclear Fusion
Nucl. Fusion **51** (2011) 053007 (16pp) doi:10.1088/0029-5515/51/5/053007

Theory of nonaxisymmetric vertical displacement events in tokamaks

R. Fitzpatrick

Institute for Fusion Studies, Department of Physics, University of Texas at Austin, Austin, TX 78712, USA

Received 12 August 2010, accepted for publication 24 February 2011
Published 13 April 2011
Online at stacks.iop.org/NF/51/053007

Abstract
A semi-analytic sharp-boundary model of a nonaxisymmetric vertical displacement event (VDE) in a large aspect-ratio, high-beta (i.e. $\beta \sim \epsilon$), vertically elongated tokamak plasma is developed. The model is used to simulate nonaxisymmetric VDEs with a wide range of different plasma equilibrium and vacuum vessel parameters. These simulations yield poloidal halo current fractions and toroidal peaking factors whose magnitudes are similar to those seen in experiments, and also reproduce the characteristic inverse scaling between the halo current fraction and the toroidal peaking factor. Moreover, the peak poloidal halo current density in the vacuum vessel is found to correlate strongly with the reciprocal of the minimum edge safety factor attained during the VDE. In addition, under certain circumstances, the ratio of the net sideways force acting on the vacuum vessel to the net vertical force is observed to approach unity. Finally, the peak vertical force per unit area acting on the vessel is found to have a strong correlation with the equilibrium toroidal plasma current at the start of the VDE, but is also found to increase with increasing vacuum vessel resistivity relative to the scrape-off layer plasma.

1. Introduction

The *tokamak* [1] is generally regarded as the magnetic confinement concept that is most likely to demonstrate controlled thermonuclear fusion in the near future. However, in order to attain this goal, a tokamak must operate *simultaneously* at high plasma pressure (which translates to good reactor economy), high plasma current (which translates to good energy confinement) and an edge safety-factor greater than 2 (which translates to good kink stability). Such operation necessitates that the plasma poloidal cross-section be *highly elongated* in the vertical direction. Unfortunately, an elongated tokamak plasma is unstable to toroidally symmetric vertical displacements [2]. In practice, it is possible to control this so-called *vertical instability* by means of a feedback system that employs an externally generated poloidal magnetic field to neutralize the plasma motion [3]. However, there are circumstances in which such a control system can fail: for instance, if a large amplitude internal plasma disturbance causes a sudden change in the plasma pressure or inductance, if the growth rate of the instability becomes larger than the bandwidth of the controller, or if the size of the required control field exceeds the capabilities of the power supply. Failure of the vertical feedback system allows the plasma to move upwards, or downwards, and eventually strike the vacuum vessel, triggering a rapid quench of the plasma pressure and current. This scenario is known as a *vertical displacement event* (VDE) [4–10].

As a vertically unstable tokamak plasma interacts with the vacuum vessel its outermost regions are scraped off, forming a so-called *halo* in which magnetic flux-surfaces are occupied partly by a relatively cool scrape-off layer (SOL) plasma, and partly by a section of the vacuum vessel. The comparatively hot main plasma is contained within the last closed magnetic flux-surface (LCFS), which is defined as the outermost flux-surface that does not intersect the vacuum vessel. The poloidal cross-section of the LCFS gradually shrinks in size as the vertical instability develops, and more and more of the main plasma is scraped off by the vacuum vessel. However, if this shrinkage takes place faster than the characteristic L/R time of the main plasma (i.e. faster than the toroidal plasma current can decay) then it causes a reduction in the safety factor, $q_{\rm p}$, at the LCFS. Moreover, such a reduction inevitably triggers a toroidally asymmetric *kink instability* when $q_{\rm p}$ falls significantly below 2 [11]. (An alternative hypothesis, not considered in this paper, is that the toroidal asymmetry seen in VDEs is caused by an intrinsic plasma–wall instability [12].)

The changing magnetic flux linked by the halo during a VDE induces electric currents, known as *halo currents*, that flow around the halo—partly through the SOL plasma, and partly through the vacuum vessel [8, 13]. (In this paper, it is assumed that halo current loops generally make a great many poloidal and toroidal circuits of the plasma, but eventually close on themselves. Current in such loops can only be driven inductively, since the electrostatic potential difference around a closed circuit is identically zero.) Now, the SOL plasma is

subject to strong cooling via direct parallel heat transport to the vacuum vessel, and thus has a comparatively low pressure, which implies that it is essentially *force-free*. Consequently, halo currents are constrained to flow *parallel* to magnetic field lines in the SOL plasma. However, there is no such restriction when the currents flow through the rigid vacuum vessel. Indeed, we would generally expect halo currents to flow through the vessel along the path of least electrical resistance (especially, in the case in which the vacuum vessel is much more resistive than the SOL plasma.) This implies that the path taken by halo currents through the vacuum vessel is predominately *poloidal*.

The interaction of the poloidal component of the halo current flowing through the vacuum vessel with the predominately toroidal magnetic field of a tokamak produces a *vertical force* of sufficient magnitude to cause a measurable vessel displacement. Halo current forces are a serious issue in the design of the ITER tokamak [14] because the scaling of such forces with machine size is extremely unfavourable for large devices. Of particular concern is the fact that when the kink mode becomes unstable, in addition to the vertical mode, during a VDE, the distribution of halo currents—and, by implication, the distribution of halo current forces—becomes strongly *toroidally asymmetric*. This phenomena leads to the alarming possibility of halo current forces becoming concentrated in a relatively small section of the vacuum vessel. Such a concentration could very easily generate a force density of sufficient magnitude to seriously damage the vessel. Another major concern is the generation of a net *sideways force* on the vacuum vessel by a nonaxisymmetric halo current force distribution.

The aim of this paper is to derive an essentially *analytic* model of a nonaxisymmetric VDE in a vertically elongated tokamak plasma. The model in question is a major extension of the simple model presented in [15], and employs a large aspect-ratio, high-beta (i.e. $\beta \sim \epsilon$, rather than $\beta \sim \epsilon^2$), *sharp-boundary* plasma equilibrium [12, 16, 17] in which the perturbed edge pressure balance is modified in response to the halo current force exerted on the section of the vacuum vessel that is in direct electrical contact with the main plasma [15, 18]. The angular boundaries of this plasma-touching section are determined self-consistently from the calculated amplitudes of the $n = 0$ (vertical) and $n = 1$ (kink) plasma displacements. (Here, n is the toroidal mode number). Furthermore, the halo current is determined from circuit analysis [8, 13], rather than relying on the simplistic assumption that the plasma current is passively convected into the vacuum vessel [19]. The latter assumption is unrealistic because, in reality, when the plasma reaches the vacuum vessel it is neutralized—*i.e.* there is no physical penetration of plasma into the vessel. Finally, the determination of the inductive voltages driving the halo current makes use of the calculated linear growth rates of the $n = 0$ and $n = 1$ modes [12, 15–20], instead of assumed growth rates [8, 13].

2. Plasma equilibrium

2.1. Coordinates

It is convenient to define the right-handed orthogonal curvilinear coordinates μ, ν, ϕ. Here, the 'radial' coordinate μ labels a set of nested axisymmetric toroidal surfaces, with $\mu = 0$ corresponding to the innermost (zero volume) surface, and $\mu = \infty$ to the outermost (infinite volume) surface. Furthermore, ν is an angle-like variable in the poloidal plane, with $\nu = 0$ and $\nu = \pi/2$ corresponding to the outboard midplane and top of the plasma, respectively. Finally, ϕ is a conventional toroidal angle.

It is also convenient to define horizontal and vertical Cartesian coordinates, x and z, respectively, in the poloidal plane, where

$$x = a\, s\, (\kappa^2 - 1)^{1/2}\, \sinh\mu\, \cos\nu, \tag{1}$$

$$z = a\, s\, (\kappa^2 - 1)^{1/2}\, \cosh\mu\, \sin\nu. \tag{2}$$

Finally, it is helpful to define the fixed right-handed Cartesian coordinates X, Y, Z, where

$$X = x\, \cos\phi, \tag{3}$$

$$Y = x\, \sin\phi, \tag{4}$$

$$Z = z. \tag{5}$$

Let $x = z = 0$ correspond to the centroid of the main plasma in the poloidal plane. Suppose that the main plasma occupies the toroidal region $\mu \leqslant \mu_{\rm p}$, so that the last closed magnetic flux-surface (LCFS) (i.e. the last flux-surface occupied entirely by plasma) corresponds to $\mu = \mu_{\rm p}$. Let $\mu_{\rm p} = \tanh^{-1}(\kappa^{-1})$, where $\kappa > 1$. The parametric equation of the LCFS in the poloidal plane is thus

$$x = a\, s\, \cos\nu, \tag{6}$$

$$z = \kappa\, a\, s\, \sin\nu. \tag{7}$$

It follows that the poloidal cross-section of the LCFS is a *vertically elongated ellipse* of elongation κ, horizontal semi-axis $s\, a$, and vertical semi-axis $\kappa\, s\, a$. Furthermore, by varying the dimensionless scale factor s from 1 to 0, we can simulate the shrinkage of the LCFS cross-section as the plasma interacts with the vacuum vessel during a VDE. For the sake of simplicity, this shrinkage is assumed to take place at constant plasma major radius, R. Note that a is the initial horizontal semi-axis of the LCFS.

It is easily demonstrated that $\nabla\mu \cdot \nabla\nu = 0$, $\nabla^2\mu = \nabla^2\nu = 0$, $|\nabla\mu| = |\nabla\nu| = (a\, h)^{-1}$, and $|\nabla\phi| = R^{-1}$, where

$$h(\mu, \nu) = s\, (\kappa^2 - 1)^{1/2}\, (\sinh^2\mu + \cos^2\nu)^{1/2}. \tag{8}$$

Now, a general vector can be written

$$\boldsymbol{A} = A_\mu\, \boldsymbol{e}_\mu + A_\nu\, \boldsymbol{e}_\nu + A_\phi\, \boldsymbol{e}_\phi, \tag{9}$$

where $\boldsymbol{e}_\mu \equiv \nabla\mu/|\nabla\mu|$, etc. The following identities are useful:

$$\nabla f \equiv (a\, h)^{-1}\, \frac{\partial f}{\partial \mu}\, \boldsymbol{e}_\mu + (a\, h)^{-1}\, \frac{\partial f}{\partial \nu}\, \boldsymbol{e}_\nu + R^{-1}\, \frac{\partial f}{\partial \phi}\, \boldsymbol{e}_\phi, \tag{10}$$

$$\nabla \cdot \boldsymbol{A} \equiv (a\, h)^{-2}\, \frac{\partial (a\, h\, A_\mu)}{\partial \mu} + (a\, h)^{-2}\, \frac{\partial (a\, h\, A_\nu)}{\partial \nu} + R^{-1}\, \frac{\partial A_\phi}{\partial \phi}, \tag{11}$$

$$\nabla\times\boldsymbol{A}\equiv\left[(a\,h)^{-1}\,\frac{\partial A_\phi}{\partial\nu}-R^{-1}\,\frac{\partial A_\nu}{\partial\phi}\right]\boldsymbol{e}_\mu + \left[-(a\,h)^{-1}\,\frac{\partial A_\phi}{\partial\mu}+R^{-1}\,\frac{\partial A_\mu}{\partial\phi}\right]\boldsymbol{e}_\nu + \left[(a\,h)^{-2}\,\frac{\partial(a\,h\,A_\nu)}{\partial\mu}-(a\,h)^{-2}\,\frac{\partial(a\,h\,A_\mu)}{\partial\nu}\right]\boldsymbol{e}_\phi, \tag{12}$$

$$\nabla^2 f\equiv(a\,h)^{-2}\,\frac{\partial^2 f}{\partial\mu^2}+(a\,h)^{-2}\,\frac{\partial^2 f}{\partial\nu^2}+R^{-2}\,\frac{\partial^2 f}{\partial\phi^2}, \tag{13}$$

$$\boldsymbol{e}_\mu\cdot(\boldsymbol{e}_\mu\cdot\nabla)\boldsymbol{A}\equiv(a\,h)^{-1}\,\frac{\partial A_\mu}{\partial\mu}+(a\,h)^{-2}\,\frac{\partial(a\,h)}{\partial\nu}\,A_\nu. \tag{14}$$

Furthermore, it can be demonstrated that

$$\boldsymbol{e}_X\cdot\boldsymbol{e}_\mu|_{\mu=\mu_{\rm p}}=\frac{h_{\rm p}(0)}{h_{\rm p}}\,\cos\nu\,\cos\phi, \tag{15}$$

$$\boldsymbol{e}_Z\cdot\boldsymbol{e}_\mu|_{\mu=\mu_{\rm p}}=\frac{h_{\rm p}(\pi/2)}{h_{\rm p}}\,\sin\nu, \tag{16}$$

where $\boldsymbol{e}_X=\nabla X/|\nabla X|$, $\boldsymbol{e}_Z\equiv\nabla Z/|\nabla Z|$, and

$$h_{\rm p}(\nu)\equiv h(\mu_{\rm p},\nu)=s\left[1+(\kappa^2-1)\,\cos^2\nu\right]^{1/2}. \tag{17}$$

Here, $h_{\rm p}(\nu)$ is a dimensionless metric function which is defined such that the length of a poloidal section of the plasma boundary lying between ν and $\nu+{\rm d}\nu$ is $a\,h_{\rm p}(\nu)\,{\rm d}\nu$.

2.2. Equilibrium pressure balance

For the sake of simplicity, all currents in the main plasma are assumed to flow immediately inside the LCFS. In reality, of course, the currents are distributed throughout the main plasma. This approximation is only reasonable in situations in which the stability of the vertical and kink instabilities responsible for the VDE depends on the plasma elongation, pressure and the edge-safety factor, but is not strongly affected by *current gradients* within the plasma (since such gradients are not captured in a sharp-boundary model). This is most likely to be the case for strongly elongated, high-beta (i.e. $\beta\sim\epsilon$, rather than $\beta\sim\epsilon^2$) plasmas. Another disadvantage of the sharp-boundary approach is that the plasma self-inductance is constrained to take a fairly low value.

Let P be the *uniform* pressure within the main plasma, and let $\boldsymbol{B}$ and $\boldsymbol{B}'$ be the equilibrium magnetic fields in the regions interior and exterior to the LCFS, respectively. It follows that

$$B_\phi=\frac{B_\iota}{1+x/R}, \tag{18}$$

$$B'_\phi=\frac{B_{\rm o}}{1+x/R}, \tag{19}$$

where B_ι and $B_{\rm o}$ are constants. Since there are no internal plasma currents, $B_\mu=B_\nu=0$. Moreover, $B'_\mu=0$ and $B'_\nu\equiv B_{\rm p}(\nu)$ immediately outside the LCFS. Finally, making use of equations (8), (11) and (12), $\nabla\cdot\boldsymbol{B}'=0$ yields

$$\left.\frac{\partial B'_\mu}{\partial\mu}\right|_{\mu=\mu_{\rm p}}=-(a\,h_{\rm p})^{-1}\,\frac{\partial(a\,h_{\rm p}\,B_{\rm p})}{\partial\nu}, \tag{20}$$

whilst $\nabla\times\boldsymbol{B}'=\boldsymbol{0}$ gives

$$\left.\frac{\partial B'_\nu}{\partial\mu}\right|_{\mu=\mu_{\rm p}}=-\,(a\,h_{\rm p})^{-1}\,B_{\rm p}\,\left.\frac{\partial(a\,h)}{\partial\mu}\right|_{\mu=\mu_{\rm p}}=-\frac{s^2\,\kappa}{h_{\rm p}^2}\,B_{\rm p}. \tag{21}$$

Equilibrium pressure balance across the LCFS leads to the relation [12, 15–17, 20]

$$P+\frac{1}{2\mu_0}\left(\frac{B_\iota}{1+\epsilon\,s\,\cos\nu}\right)^2=\frac{1}{2\mu_0}\left(\frac{B_{\rm o}}{1+\epsilon\,s\,\cos\nu}\right)^2+\frac{B_{\rm p}^2}{2\mu_0}, \tag{22}$$

where $\epsilon=a/R\ll1$. This relation can also be written

$$\beta+\left[\left(\frac{B_\iota}{B_{\rm o}}\right)^2-1\right]\frac{1}{(1+\epsilon\,s\,\cos\nu)^2}=\frac{B_{\rm p}^2}{B_{\rm o}^2}, \tag{23}$$

where $\beta=2\mu_0\,P/B_{\rm o}^2$ is the *toroidal plasma beta*. Assuming that $\beta\sim\epsilon$, $B_{\rm o}-B_\iota\sim\epsilon\,B_{\rm o}$, and $B_\iota^2/B_{\rm o}^2-1+\beta=A\,\epsilon^2$, where A is an $\mathcal{O}(1)$ constant, we obtain

$$\frac{B_{\rm p}}{\epsilon\,B_{\rm o}}=\left(A+2\,s\,\frac{\beta}{\epsilon}\,\cos\nu\right)^{1/2}+\mathcal{O}(\epsilon), \tag{24}$$

$$B_{\rm o}-B_\iota=\frac{\beta}{2}\,B_{\rm o}+\mathcal{O}(\epsilon^2). \tag{25}$$

Finally, the net toroidal plasma current is written

$$\mu_0\,I_{\phi\,{\rm p}}=\oint B_{\rm p}\,a\,h_{\rm p}\,{\rm d}\nu, \tag{26}$$

whereas the magnetic winding number, or safety factor, on the LCFS becomes

$$q_{\rm p}=\oint\frac{\epsilon\,B_{\rm o}}{B_{\rm p}}\,h_{\rm p}\,\frac{{\rm d}\nu}{2\pi}. \tag{27}$$

Note that the adopted plasma equilibrium assumes the high-beta ordering $\beta\sim\epsilon$. However, the equilibrium is also consistent with the low-beta ordering $\beta\sim\epsilon^2$ when $\hat{\beta}\equiv\beta/\epsilon=0$.

3. Halo physics

3.1. Structure of Halo

The halo is a (radially) thin, annular, toroidal region situated just outside the LCFS. Magnetic flux-surfaces in the halo are occupied partly by *force-free* SOL plasma, and partly by a section of the vacuum vessel that is in electrical contact with the main plasma. This section is henceforth referred to as the 'limiter', and the rest of the vacuum vessel is referred to as the 'wall'. It is assumed that the limiter lies directly above the main plasma, and is brought into electrical contact with it via the action of an *upward vertical instability*.

It is helpful to define the 'straight' poloidal angle

$$\theta(\nu)=\frac{1}{q_{\rm p}}\int_{\pi/2}^{\nu}\frac{\epsilon\,B_{\rm o}}{B_{\rm p}}\,h_{\rm p}\,{\rm d}\nu, \tag{28}$$

where $\theta=0$ corresponds to $\nu=\pi/2$. The angular equation of an equilibrium magnetic field line in the halo is thus

$$\frac{{\rm d}\phi}{{\rm d}\theta}=q_{\rm p}. \tag{29}$$

Furthermore,

$$|\nabla\theta|^{-1}=\frac{{\rm d}\nu}{{\rm d}\theta}\,|\nabla\nu|^{-1}=a\,\frac{B_{\rm p}}{\epsilon\,B_{\rm o}}\,q_{\rm p}. \tag{30}$$

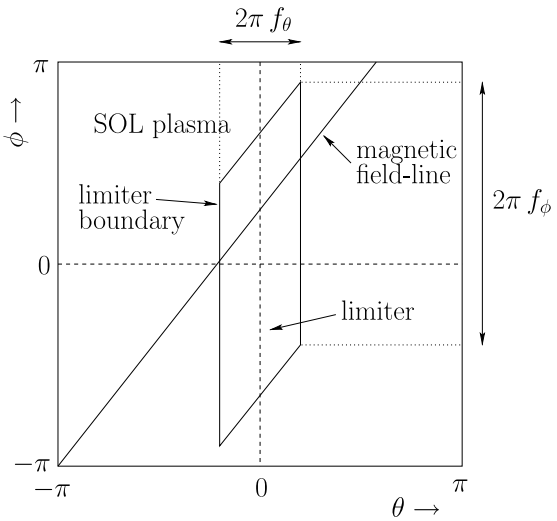

Figure 1. Schematic diagram showing structure of halo.

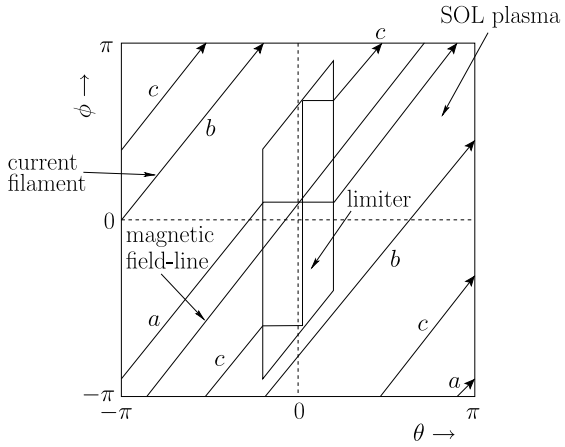

Figure 2. Schematic diagram of class-1 halo current pattern showing type-a, -b and -c, poloidal turns.

Note that

$$\theta \simeq c\,(\nu - \pi/2) \tag{31}$$

in the vicinity of $\theta = 0$, and

$$\left.\frac{B_{\rm p}}{B_{\rm o}}\right|_{\theta=0} = \frac{\epsilon\, s}{c\, q_{\rm p}}, \tag{32}$$

where $c = s/(A^{1/2}\, q_{\rm p})$.

Let the angular boundaries of the limiter be

$$\theta_- \leqslant \theta \leqslant \theta_+, \tag{33}$$

and

$$\phi_- \leqslant \phi \leqslant \phi_+, \tag{34}$$

where $\theta_\pm = \pm\pi\ f_\theta$ and $\phi_\pm = \pm\pi\ f_\phi + q_{\rm p}\,\theta$. Here, f_θ and f_ϕ (where $0 \leqslant f_\theta \leqslant 1$ and $0 \leqslant f_\phi \leqslant 1$) are the fractional angular poloidal and toroidal coverages of the limiter, respectively. Any toroidal asymmetry (i.e. $f_\phi < 1$) of the limiter boundaries is due to the action of a nonaxisymmetric *kink instability*. For the sake of simplicity, the limiter boundaries are assumed to run either in the *toroidal* direction or *parallel* to equilibrium magnetic field lines. See figure 1.

By definition, *halo currents* flow partly through the SOL plasma, and partly through the limiter. Furthermore, halo currents are required to flow *parallel* to equilibrium magnetic field lines in the force-free SOL plasma, but can flow in *any* direction in the rigid limiter. In the following, our discussion is restricted to *two* fundamental classes of halo current pattern. A general halo current pattern can be formed from an appropriate linear combination of these two patterns.

3.2. Class-1 halo currents

A class-1 halo current pattern is such that the current flows *parallel* to magnetic field lines in the SOL plasma, but flows *poloidally* in the limiter (in order to minimize the electrical resistance of a halo current filament). Now, an 'ergodic' class-1 halo current filament (i.e. a filament which only closes after a great many poloidal turns) consists of *three* distinct types of poloidal turn. A type-a turn passes through the middle of the limiter. A type-b turn runs entirely through the SOL plasma. Finally, a type-c turn passes through both toroidal edges of the limiter, and is completed by a toroidal leg which runs through the limiter (in the $+\phi$ direction). (The toroidal leg is required in order to obtain a complete mapping of current filaments from $\theta = -\pi$ to $\theta = +\pi$.) See figure 2. It is evident that the fraction of poloidal turns which are of type-a is $f_a = f_\phi - q_{\rm p}\, f_\theta$, whereas the fraction which are of type-b is $f_b = 1 - f_\phi$, and the fraction which are of type-c is $f_c = q_{\rm p}\, f_\theta$. Moreover, the change in ϕ associated with each type of turn is

$$\frac{\Delta\phi_a}{2\pi} = q_{\rm p}\,(1 - f_\theta), \tag{35}$$

$$\frac{\Delta\phi_b}{2\pi} = q_{\rm p}, \tag{36}$$

$$\frac{\Delta\phi_c}{2\pi} = q_{\rm p}\,(1 - f_\theta) + f_\phi. \tag{37}$$

Hence, the mean magnetic winding number of an ergodic class-1 halo current filament is

$$q_{\rm p\,1} = f_a\,\frac{\Delta\phi_a}{2\pi} + f_b\,\frac{\Delta\phi_b}{2\pi} + f_c\,\frac{\Delta\phi_c}{2\pi} = q_{\rm p}. \tag{38}$$

Note that a class-1 halo current pattern is topologically equivalent to one in which the halo current flows parallel to magnetic field lines both in the limiter and the SOL plasma. Hence, we would not expect a class-1 pattern to generate a force on the limiter. Incidentally, in this paper, we are neglecting 'resonant' halo current filaments, which close after a few poloidal turns, because such filaments are only important at a relatively small number of special values of $q_{\rm p}$ (particularly, in the limit in which the vacuum vessel is much more resistive than the SOL plasma).

Let $w_\parallel$, w_θ and w_ϕ be the width (within a magnetic flux-surface: i.e. at constant μ) of a given ergodic class-1 halo current filament as it passes parallel to magnetic field lines through the SOL plasma, poloidally through the limiter, and toroidally through the limiter, respectively. Furthermore, let δ be the radial (i.e. at constant θ and ϕ) thickness of the filament.

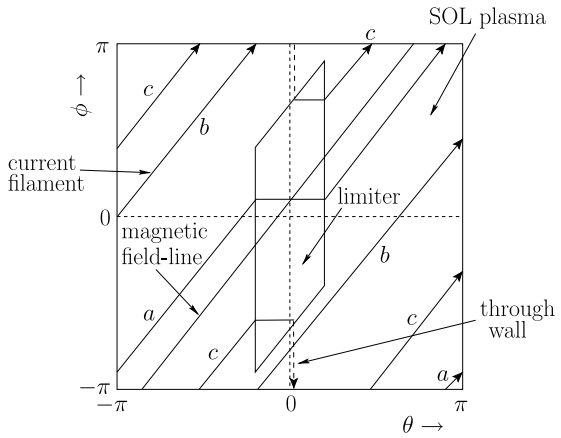

Figure 3. Schematic diagram of class-2 halo current pattern showing type-a, -b, and -c, poloidal turns.

It follows from geometry, and the fact that the filament is bounded by magnetic field lines in the SOL plasma, that

$$w_\phi(\theta) \simeq w_\parallel(\theta) = [B_{\rm p}(\theta)/B_{\rm p}(0)]\, w_0, \tag{39}$$

$$w_\theta \simeq [B_{\rm o}/B_{\rm p}(0)]\, w_0, \tag{40}$$

where w_0 is a constant. It is convenient to assume that $\delta(\theta) = [B_{\rm p}(0)/B_{\rm p}(\theta)]\,\delta_0$, where $\delta_0 \ll a$ is a constant. Note that $\delta(\theta)$ represents the radial thickness of both the SOL plasma and the limiter/wall. Let $j_{\parallel 1}$, $j_{\theta 1}$ and $j_{\phi 1}$ be the filament current density as it runs parallel to magnetic field lines through the SOL plasma, poloidally through the limiter, and toroidally through the limiter, respectively. Charge conservation yields $j_{\parallel 1}\, w_\parallel\, \delta = j_{\theta 1}\, w_\theta\, \delta = j_{\phi 1}\, w_\phi\, \delta =$ const., which implies that $j_{\parallel 1}$ is constant, $j_{\phi 1} \simeq j_{\parallel 1}$, and $j_{\theta 1} \simeq [B_{\rm p}(\theta)/B_{\rm o}]\, j_{\parallel 1}$.

3.3. Class-2 halo currents

An ergodic class-2 halo current pattern is similar to a class-1 pattern, except that a type-c poloidal turn is completed by a toroidal leg which runs (in the $-\phi$ direction) through that part of the wall lying between $\theta = \theta_-$ and $\theta = \theta_+$, rather than through the limiter. (As before, the toroidal leg is required in order to obtain a complete mapping of current filaments from $\theta = -\pi$ to $\theta = +\pi$.) See figure 3. The fraction of poloidal turns which are of type-a, -b and -c is the same as for class-1 patterns. Moreover, the change in ϕ associated with each type of turn is also the same as for class-1 patterns, except that

$$\frac{\Delta\phi_c}{2\pi} = q_{\rm p}\,(1 - f_\theta) - (1 - f_\phi). \tag{41}$$

Hence, the effective magnetic winding number of an ergodic class-2 halo current filament is

$$q_{\rm p\,2} = f_a\,\frac{\Delta\phi_a}{2\pi} + f_b\,\frac{\Delta\phi_b}{2\pi} + f_c\,\frac{\Delta\phi_c}{2\pi} = q_{\rm p}\,(1 - f_\theta). \tag{42}$$

Note that in a class-2 halo current pattern the current in the limiter does not flow parallel to the magnetic field. Hence, such a pattern can generate a force on the limiter.

Let $j_{\parallel 2}$, $j_{\theta 2}$ and $-j_{\phi 2}$ be the filament current density as it runs parallel to magnetic field lines through the SOL plasma, poloidally through the limiter, and toroidally through the wall (in the minus-ϕ direction), respectively. Charge conservation yields $j_{\parallel 2}\, w_\parallel\, \delta = j_{\theta 2}\, w_\theta\, \delta = -j_{\phi 2}\, w_\phi\, \delta =$ const., which implies that $j_{\parallel 2}$ is constant, $-j_{\phi 2} \simeq j_{\parallel 2}$, and $j_{\theta 2} \simeq [B_{\rm p}(\theta)/B_{\rm o}]\, j_{\parallel 2}$.

3.4. Potential drops across current filaments

Consider an ergodic class-1 halo current filament. The potential drop across a type-a poloidal turn is

$$V_{1\,a} \simeq \int_{\theta_+}^{\theta_-} \frac{({\rm d}\phi/{\rm d}\theta)\,{\rm d}\theta}{|\nabla\phi|}\,\frac{j_{\parallel 1} + j_{\parallel 2}}{\sigma_{\rm s}} + \int_{\theta_-}^{\theta_+} \frac{{\rm d}\theta}{|\nabla\theta|}\,\frac{j_{\theta 1} + j_{\theta 2}}{\sigma_{\rm l}}$$
$$\simeq 2\pi\, R\, q_{\rm p}\left[\frac{1 - f_\theta}{\sigma_{\rm s}\,\delta_0} + \left(\frac{\epsilon\, s}{c\, q_{\rm p}}\right)^2 \frac{f_\theta}{\sigma_{\rm l}\,\delta_0}\right](\imath_{\parallel 1} + \imath_{\parallel 2}), \tag{43}$$

where $\sigma_{\rm s}$ and $\sigma_{\rm l}$ are the (uniform) electrical conductivities of the SOL plasma and the limiter/wall, respectively, and $\imath_{\parallel 1,2} = j_{\parallel 1,2}\,\delta_0$. Here, $\imath_{\parallel 1}$ and $\imath_{\parallel 2}$ are the radially integrated halo current densities per unit length associated with class-1 and class-2 halo current patterns, respectively, as they run parallel to magnetic field lines through the SOL plasma. Moreover, we have assumed that $\epsilon/q_{\rm p} \ll 1$ and $f_\theta \ll 1$. The potential drop across a type-b poloidal turn is

$$V_{1\,b} \simeq \oint \frac{({\rm d}\theta/{\rm d}\phi)\,{\rm d}\theta}{|\nabla\phi|}\,\frac{j_{\parallel 1} + j_{\parallel 2}}{\sigma_{\rm s}} = 2\pi\, R\, q_{\rm p}\,\frac{\imath_{\parallel 1} + \imath_{\parallel 2}}{\sigma_{\rm s}\,\delta_0}. \tag{44}$$

Finally, the potential drop across a type-c poloidal turn is

$$V_{1\,c} = V_{1\,a} + \int_{\phi_-}^{\phi_+} \frac{{\rm d}\phi}{|\nabla\phi|}\,\frac{j_{\phi 1}}{\sigma_{\rm l}} = V_a + 2\pi\, R\, f_\phi\,\frac{\imath_{\parallel 1}}{\sigma_{\rm l}\,\delta_0}. \tag{45}$$

Thus, the mean potential drop across a single poloidal turn of an ergodic class-1 halo current filament is

$$V_1 = f_a\, V_{1\,a} + f_b\, V_{1\,b} + f_c\, V_{1\,c}$$
$$\simeq \frac{2\pi\, R\, q_{\rm p}}{\sigma_{\rm l}\,\delta_0}[(1 - f_\theta\, f_\phi)\,\tau\,(\imath_{\parallel 1} + \imath_{\parallel 2}) + f_\theta\, f_\phi\,\imath_{\parallel 1}], \tag{46}$$

where $\tau = \sigma_{\rm l}/\sigma_{\rm s}$. Here, we have again assumed that $\epsilon/q_{\rm p} \ll 1$.

Consider an ergodic class-2 halo current filament. The potential drop across a type-a poloidal turn is such that $V_{2\,a} = V_{1\,a}$. Likewise, the potential drop across a type-b poloidal turn is such that $V_{2\,b} = V_{1\,b}$. Finally, the potential drop across a type-c poloidal turn is written

$$V_{2\,c} = V_{2\,a} + \int_{\phi_+}^{\phi_-} \frac{{\rm d}\phi}{|\nabla\phi|}\,\frac{-j_{\phi 2}}{\sigma_{\rm l}} = V_{2\,a} + 2\pi\, R\,(1 - f_\phi)\,\frac{\imath_{\parallel 2}}{\sigma_{\rm l}\,\delta_0}. \tag{47}$$

Thus, the mean potential drop across a single poloidal turn of an ergodic class-2 halo current filament is

$$V_2 = f_a\, V_{2\,a} + f_b\, V_{2\,b} + f_c\, V_{2\,c}$$
$$\simeq \frac{2\pi\, R\, q_{\rm p}}{\sigma_{\rm l}\,\delta_0}[(1 - f_\theta\, f_\phi)\,\tau\,(\imath_{\parallel 1} + \imath_{\parallel 2}) + f_\theta\,(1 - f_\phi)\,\imath_{\parallel 2}]. \tag{48}$$

3.5. Halo current circuit equations

The halo currents discussed in this paper are driven *inductively* by the changing toroidal and poloidal magnetic fluxes linked by the halo as the cross-sectional area of the LCFS shrinks. Now, the toroidal flux linked by the halo is

$$\Phi_\phi \simeq \pi\,\kappa\, a^2\, s^2\, B_\imath. \tag{49}$$

Thus, the single-turn poloidal emf generated in the halo by the shrinkage of the LCFS is

$$\mathcal{E}_\theta = -\frac{\mathrm{d}\,\Phi_\phi}{\mathrm{d}t} \simeq \pi\, a^2\, B_\mathrm{o}[2\,\kappa + p_\kappa\,(\kappa-1) - p_\beta\,\kappa\,\beta/2]s^2\,\gamma, \tag{50}$$

assuming that

$$\frac{\mathrm{d}\ln s}{\mathrm{d}t} = -\gamma, \tag{51}$$

where γ is the growth rate of the instability causing the shrinkage, and

$$p_\kappa = \frac{\mathrm{d}\ln(\kappa-1)}{\mathrm{d}\ln s}, \tag{52}$$

$$p_\beta = \frac{\mathrm{d}\ln\beta}{\mathrm{d}\ln s}. \tag{53}$$

Here, use has been made of equation (25). Furthermore, the poloidal flux linked by the halo is

$$\Phi_\theta = L_\mathrm{p}\, I_{\phi\,\mathrm{p}}, \tag{54}$$

where

$$L_\mathrm{p} \simeq \mu_0\, R\left[\ln\left(\frac{8}{\epsilon\, s}\right) - 2\right] \tag{55}$$

is the (approximate) self-inductance of the shrinking plasma. Hence, the single-turn toroidal emf generated in the halo by the shrinkage of the LCFS is

$$\begin{aligned}\mathcal{E}_\phi &= -\frac{\mathrm{d}\Phi_\theta}{\mathrm{d}t}\\ &= \mu_0\, R\left(p_I\left[\ln\left(\frac{8}{\epsilon\, s}\right) - 2\right] - 1\right) I_{\phi\,\mathrm{p}}\,\gamma,\end{aligned} \tag{56}$$

where

$$p_I = \frac{\mathrm{d}\ln I_{\phi\,\mathrm{p}}}{\mathrm{d}\ln s}. \tag{57}$$

The circuit equation for a single poloidal turn of an ergodic class-1 halo current filament is simply

$$\mathcal{E}_\theta + q_{\mathrm{p}\,1}\,\mathcal{E}_\phi = V_1. \tag{58}$$

Likewise, the circuit equation for a single poloidal turn of an ergodic class-2 halo current filament takes the form

$$\mathcal{E}_\theta + q_{\mathrm{p}\,2}\,\mathcal{E}_\phi = V_2. \tag{59}$$

According to the above circuit equations, class-1 and class-2 halo current filaments essentially act like helical wires, with slightly different mean helical pitches, which are linked by both toroidal and poloidal magnetic flux. It follows from equations (38), (42), (46), (48), (50) and (56) that

$$\begin{aligned}&[f_\theta\, f_\phi + (1-f_\theta\, f_\phi)\,\tau]\hat{\imath}_{\parallel\,1} + (1-f_\theta\, f_\phi)\,\tau\,\hat{\imath}_{\parallel\,2}\\ &\quad= \frac{\hat{\gamma}}{2\pi}(\mathcal{C}_\theta + \mathcal{C}_\phi),\end{aligned} \tag{60}$$

$$\begin{aligned}&(1-f_\theta\, f_\phi)\,\tau\,\hat{\imath}_{\parallel\,1} + [f_\theta\,(1-f_\phi) + (1-f_\theta\, f_\phi)\,\tau]\hat{\imath}_{\parallel\,2}\\ &\quad= \frac{\hat{\gamma}}{2\pi}(\mathcal{C}_\theta + [1-f_\theta]\,\mathcal{C}_\phi),\end{aligned} \tag{61}$$

where

$$\mathcal{C}_\theta = \pi[2\,\kappa + p_\kappa\,(\kappa-1) - p_\beta\,\kappa\,\beta/2]\frac{s^2}{q_\mathrm{p}}, \tag{62}$$

$$\mathcal{C}_\phi = \left(p_I\left[\ln\left(\frac{8}{\epsilon\, s}\right) - 2\right] - 1\right)\hat{I}_{\phi\,\mathrm{p}}, \tag{63}$$

$\hat{\imath}_{\parallel\,1,2} = \imath_{\parallel\,1,2}/(\epsilon B_\mathrm{o}/\mu_0)$, $\hat{I}_{\phi\,\mathrm{p}} = I_{\phi\,\mathrm{p}}/(a\,\epsilon B_\mathrm{o}/\mu_0)$ and $\hat{\gamma} = \gamma\,\tau_l$. Here, ϵB_o is a typical equilibrium poloidal field-strength, $a\,\epsilon B_0/\mu_0$ is a typical equilibrium toroidal plasma current, $\epsilon B_\mathrm{o}/\mu_0$ is a typical radially integrated equilibrium toroidal plasma current per unit poloidal length, and $\tau_l = \mu_0\,\sigma_\mathrm{l}\,\delta_0\,a$ is the characteristic L/R time of the limiter/wall. All hatted quantities are designed to be $\mathcal{O}(1)$. Equations (60) and (61) can be inverted to give

$$\hat{\imath}_{\parallel\,1} = \frac{\hat{\gamma}}{2\pi}\left[\frac{(1-f_\phi)\,(\mathcal{C}_\theta + \mathcal{C}_\phi) + (1-f_\theta\, f_\phi)\,\tau\,\mathcal{C}_\phi}{f_\theta\, f_\phi\,(1-f_\phi) + (1-f_\theta\, f_\phi)\,\tau}\right], \tag{64}$$

$$\hat{\imath}_{\parallel\,2} = \frac{\hat{\gamma}}{2\pi}\left[\frac{f_\phi\,(\mathcal{C}_\theta + [1-f_\theta]\,\mathcal{C}_\phi) - (1-f_\theta\, f_\phi)\,\tau\,\mathcal{C}_\phi}{f_\theta\, f_\phi\,(1-f_\phi) + (1-f_\theta\, f_\phi)\,\tau}\right]. \tag{65}$$

3.6. Poloidal halo current

The net poloidal halo current flowing through the limiter is

$$I_{\theta\,1} = \int_{\phi_-}^{\phi_+} \frac{\mathrm{d}\phi}{|\nabla\phi|}\,(J_{\theta\,1} + J_{\theta\,2})\,\delta\Big|_{\theta=0}, \tag{66}$$

which reduces to

$$\hat{I}_{\theta\,1} = \frac{s\,\hat{\gamma}}{c\,q_\mathrm{p}}\left[\frac{f_\phi\,(\mathcal{C}_\theta + [1-f_\theta\, f_\phi]\,\mathcal{C}_\phi)}{f_\theta\, f_\phi\,(1-f_\phi) + (1-f_\theta\, f_\phi)\,\tau}\right], \tag{67}$$

where $\hat{I}_{\theta\,1} = I_{\theta\,1}/(a\,\epsilon B_\mathrm{o}/\mu_0)$. Moreover, it is easily shown that the conventional *toroidal peaking factor* for the poloidal halo current (which is defined $\mathcal{T}_\phi = \imath_{\theta\,\max}/(\oint \imath_\theta\,\mathrm{d}\phi/2\pi)$, where $\imath_\theta(\phi) = (J_{\theta\,1} + J_{\theta\,2})\,\delta|_{\theta=0}$) is

$$\mathcal{T}_\phi = \frac{1}{f_\phi} \tag{68}$$

(since $\imath_\theta$ is a constant for $\phi_- \leqslant \phi \leqslant \phi_+$, and zero otherwise).

3.7. Toroidal SOL current

The net toroidal current flowing through the SOL plasma is

$$I_{\phi\,\mathrm{s}} \simeq \int_{\theta_+}^{\theta_-} \frac{\mathrm{d}\theta}{|\nabla\theta|}\,(J_{\parallel\,1} + J_{\parallel\,2})\,\delta\Big|_{\phi=0}, \tag{69}$$

which yields

$$\hat{I}_{\phi\,\mathrm{s}} \simeq \frac{s\,\hat{\gamma}}{c}\left[\frac{(1-f_\theta)\,(\mathcal{C}_\theta + [1-f_\theta\, f_\phi]\,\mathcal{C}_\phi)}{f_\theta\, f_\phi\,(1-f_\phi) + (1-f_\theta\, f_\phi)\,\tau}\right], \tag{70}$$

where $\hat{I}_{\phi\,\mathrm{s}} = I_{\phi\,\mathrm{s}}/(a\,\epsilon B_\mathrm{o}/\mu_0)$.

3.8. Normal force on vacuum vessel

The radially integrated normal halo current *force per unit area* acting on the vacuum vessel is

$$p_\mu \simeq j_{\theta\,2}\, B_{\rm o}\, \delta\, \zeta_{\rm v} = \iota_{\parallel\,2}\, B_{\rm p}(0)\, \zeta_{\rm v}, \tag{71}$$

where

$$\zeta_{\rm v}(\theta) = \begin{cases} 1 & \theta_- \leqslant \theta \leqslant \theta_+ \\ 0 & \text{otherwise.} \end{cases}. \tag{72}$$

It follows that

$$\hat{p}_\mu \simeq \frac{s\,\hat{\gamma}}{2\pi\, c\, q_{\rm p}} \left[\frac{f_\phi\,(\mathcal{C}_\theta + [1-f_\theta]\,\mathcal{C}_\phi) - (1-f_\theta\,f_\phi)\,\tau\,C_\phi}{f_\theta\,f_\phi\,(1-f_\phi) + (1-f_\theta\,f_\phi)\,\tau} \right] \zeta_{\rm v}, \tag{73}$$

where $\hat{p}_\mu = p_\mu/(\epsilon^2 B_{\rm o}^2/\mu_0)$. Recall that only class-2 halo currents generate a force on the vacuum vessel.

The above vacuum vessel force distribution is *toroidally symmetric*, despite the fact that the distribution of poloidal halo currents is *toroidally asymmetric*, because of the presence of class-2 halo currents flowing toroidally through the section of the wall which lies between $\theta = \theta_-$ and $\theta = \theta_+$ (see figure 3). Now, the normal force density in the limiter is due to the (small) class-2 poloidal halo current density crossed with the (large) toroidal magnetic field, whereas that in the wall is due to the (large) class-2 toroidal halo current density crossed with the (small) poloidal magnetic field. Moreover, in our somewhat idealized model, these two force densities turn out to be *exactly equal*. Note, however, that our analysis has neglected the gap which inevitably develops between the main plasma and the aforementioned section of the wall when the kink mode attains a finite amplitude. In response to the gap, we would expect the toroidal current distribution in the wall to spread outside the region $\theta_- \leqslant \theta \leqslant \theta_+$ (leading to a reduction in the current density), and the equilibrium poloidal field-strength at the wall to simultaneously drop. Both these effects tend to reduce the normal force per unit area acting on the wall *relative* to that acting on the limiter. We can crudely simulate this reduction by entirely neglecting the normal force acting on the wall, whilst retaining that acting on the limiter. In other words, in the following, equation (73) is replaced by

$$\hat{p}_\mu \simeq \frac{s\,\hat{\gamma}}{2\pi\, c\, q_{\rm p}} \left[\frac{f_\phi\,(\mathcal{C}_\theta + [1-f_\theta]\,\mathcal{C}_\phi) - (1-f_\theta\,f_\phi)\,\tau\,C_\phi}{f_\theta\,f_\phi\,(1-f_\phi) + (1-f_\theta\,f_\phi)\,\tau} \right] \zeta_l, \tag{74}$$

where

$$\zeta_l(\theta,\phi) = \begin{cases} 1 & \theta_- \leqslant \theta \leqslant \theta_+ \text{ and } \phi_- \leqslant \phi \leqslant \phi_+ \\ 0 & \text{otherwise.} \end{cases} \tag{75}$$

3.9. Limiter force density

The normal halo current *force density* within the limiter is

$$f_\mu \simeq \jmath_{\theta\,2}\, B_{\rm o}\, \zeta_{\rm l} = \frac{\iota_{\parallel\,2}\, B_{\rm p}\, \zeta_{\rm l}}{\delta_0}. \tag{76}$$

It follows that

$$\hat{f}_\mu = \frac{s\,\hat{\gamma}}{2\pi\, c\, q_{\rm p}\, \hat{\delta}_0} \left[\frac{f_\phi\,(\mathcal{C}_\theta + [1-f_\theta]\,\mathcal{C}_\phi) - (1-f_\theta\,f_\phi)\,\tau\,C_\phi}{f_\theta\,f_\phi\,(1-f_\phi) + (1-f_\theta\,f_\phi)\,\tau} \right] \times \frac{B_{\rm p}}{B_{\rm p}(0)}\, \zeta_{\rm l}, \tag{77}$$

where $\hat{f}_\mu = f_\mu/(\epsilon^2\, B_{\rm o}^2/a\,\mu_0)$ and $\hat{\delta}_0 = \delta_0/a$.

3.10. Net vertical force on vacuum vessel

The net *vertical force* acting on the vacuum vessel is

$$F_{\rm v} = \oint \oint \frac{{\rm d}\nu}{|\nabla\nu|}\, \frac{{\rm d}\phi}{|\nabla\phi|}\, p_\mu \boldsymbol{e}_Z \cdot \boldsymbol{e}_\mu|_{\mu=\mu_{\rm p}}, \tag{78}$$

which reduces to

$$\hat{F}_{\rm v} \simeq \frac{2\pi\, s^2\, \hat{\gamma}}{c^2\, q_{\rm p}} \times \left[\frac{f_\theta\, f_\phi\, \{f_\phi\,(\mathcal{C}_\theta + [1-f_\theta]\,\mathcal{C}_\phi) - (1-f_\theta\,f_\phi)\,\tau\,C_\phi\}}{f_\theta\,f_\phi\,(1-f_\phi) + (1-f_\theta\,f_\phi)\,\tau} \right] \text{sinc}\,(\pi\, f_\theta/c), \tag{79}$$

where $\text{sinc}(x) \equiv \sin x/x$, $\hat{F}_{\rm v} = F_{\rm v}/(\epsilon\, a^2\, B_{\rm o}^2/\mu_0)$, and use has been made of equation (16).

3.11. Net sideways force on vacuum vessel.

Our present model predicts *zero* sideways force acting on the vacuum vessel because, for the sake of simplicity, it assumes that the vacuum vessel has the same shape and major radius as the plasma, which leads to a limiter which is poloidally symmetric about the top of the plasma (i.e. $\nu = \pi/2$). See section 5.6. This, in turn, yields a sideways force which vanishes by symmetry. In reality, however, the vacuum vessel is likely to have a different shape, and a slightly different major radius, than the plasma, leading to a poloidally asymmetric limiter, and a non-zero sideways force. We can crudely simulate this effect by assuming that the limiter extends from $\nu_- \simeq \pi/2$ to $\nu_+ \simeq \pi/2 + 2\pi\, f_\theta/c$, instead of from $\nu_- \simeq \pi/2 - \pi\, f_\theta/c$ to $\nu_+ \simeq \pi/2 + \pi\, f_\theta/c$, for the purpose of calculating the sideways force. This assumption effectively yields an upper limit on the sideways force, since it completely suppresses cancellation between the sideways components of the normal forces acting on the inboard and outboard halves of the vacuum vessel (because the limiter is shifted entirely to the outboard half, so zero normal force acts on the inboard half). Thus, the maximum net sideways force acting on the vacuum vessel, which is written

$$F_{\rm h} = (F_X^2 + F_Y^2)^{1/2} = |F_X| = \left| \oint \oint \frac{{\rm d}\nu}{|\nabla\nu|}\, \frac{{\rm d}\phi}{|\nabla\phi|}\, p_\mu\, \boldsymbol{e}_X \cdot \boldsymbol{e}_\mu \big|_{\mu=\mu_{\rm p}} \right|, \tag{80}$$

since $F_Y = 0$ by symmetry, becomes

$$\hat{F}_{\rm h} \simeq \frac{2\pi^2\, \kappa\, s^2\, \hat{\gamma}}{c^3\, q_{\rm p}} \times \left[\frac{f_\theta^2\, f_\phi\, \{f_\phi\,(\mathcal{C}_\theta + [1-f_\theta]\,\mathcal{C}_\phi) - (1-f_\theta\,f_\phi)\,\tau\,C_\phi\}}{f_\theta\,f_\phi\,(1-f_\phi) + (1-f_\theta\,f_\phi)\,\tau} \right] \text{sinc}^2(\pi\, f_\theta/c)\, \text{sinc}(\pi\, f_\phi), \tag{81}$$

where $\hat{F}_{\rm h} = F_{\rm h}/(\epsilon\, a^2\, B_{\rm o}^2/\mu_0)$, and use has been made of equation (15).

4. Plasma stability

Let us assume a common $\exp(-{\rm i}\, n\, \phi)$ toroidal variation of perturbed quantities, where n is a non-negative integer. Furthermore, let the perturbed magnetic fields inside and outside the LCFS be written $\delta\boldsymbol{B} = \nabla V$ and $\delta\boldsymbol{B}' = \nabla V'$,

respectively. This automatically ensures that the perturbed current density is zero both interior and exterior to the LCFS. (Any perturbed current is assumed to flow on the LCFS.) Furthermore, the perturbed magnetic fields are divergence-free provided that $\nabla^2 V = \nabla^2 V' = 0$, or, from (13),

$$\frac{\partial^2 V}{\partial \mu^2} + \frac{\partial^2 V}{\partial \nu^2} \simeq 0, \tag{82}$$

$$\frac{\partial^2 V'}{\partial \mu^2} + \frac{\partial^2 V'}{\partial \nu^2} \simeq 0, \tag{83}$$

assuming that $n\,\epsilon \ll 1$.

Now, in order to guarantee that $\delta \boldsymbol{B}$ is both finite and continuous at $\mu = 0$, we require [17]

$$V(0, \nu) = V(0, \pi - \nu), \tag{84}$$

$$\frac{\partial V(0, \nu)}{\partial \mu} = -\frac{\partial V(0, \pi - \nu)}{\partial \mu}. \tag{85}$$

The most general solution of (82) which satisfies these constraints is

$$V(\mu, \nu) = \sum_{m \neq 0} [a_m \cosh(m\,\mu) \cos(m\,[\nu - \pi/2]) + b_m \sinh(m\,\mu) \sin(m\,[\nu - \pi/2])], \tag{86}$$

where m is an integer, and the a_m and b_m are constants. Furthermore, the most general solution of (83) which satisfies the physical constraint $V'(\mu \to \infty, \nu) \to 0$ is

$$V'(\mu, \nu) = \sum_{m \neq 0} a'_m \, \mathrm{e}^{-|m|\,(\mu - \mu_\mathrm{p})} \, \mathrm{e}^{\mathrm{i}\,m\,\nu}, \tag{87}$$

where the a'_m are constants. (Here, we are neglecting currents flowing in that section of the wall which is remote from the plasma once significant shrinkage of the LCFS has occurred: i.e. the section which does not lie in the range $\theta_- \leqslant \theta \leqslant \theta_+$.)

The matching conditions for perturbed quantities at the LCFS are [12, 15–17]

$$\boldsymbol{e}_\mu \cdot \delta \boldsymbol{B} = \boldsymbol{B} \cdot \nabla \xi - \xi\, \boldsymbol{e}_\mu \cdot (\boldsymbol{e}_\mu \cdot \nabla) \boldsymbol{B}, \tag{88}$$

$$\boldsymbol{e}_\mu \cdot \delta \boldsymbol{B}' = \boldsymbol{B}' \cdot \nabla \xi - \xi\, \boldsymbol{e}_\mu \cdot (\boldsymbol{e}_\mu \cdot \nabla) \boldsymbol{B}', \tag{89}$$

$$\mu_0^{-1}\, \boldsymbol{B} \cdot \delta \boldsymbol{B} + \xi\, \boldsymbol{e}_\mu \cdot \nabla (B^2/2\mu_0) = \mu_0^{-1}\, \boldsymbol{B}' \cdot \delta \boldsymbol{B}' + \xi\, \boldsymbol{e}_\mu \cdot \nabla (B'^2/2\mu_0) + \xi\, f_\mu, \tag{90}$$

where $\xi(\nu)\, \exp(-\mathrm{i}\, n\, \phi)$ is the normal plasma displacement on the LCFS, and f_μ is the normal force density acting on the limiter due to the halo current (see equation (77)). The first two matching conditions ensure that the perturbed LCFS remains a magnetic flux-surface, whereas the third condition maintains perturbed pressure balance (which is necessary, since we are assuming that the growth times of the vertical and kink instabilities are both much longer than the Alfvén time). The final term on the right-hand side of equation (90) can be shown to be the net normal force per unit area (due to plasma pressure and $\boldsymbol{j} \times \boldsymbol{B}$ forces) acting outwards across the plasma boundary. Of course, for a free-boundary plasma (that is not moving Alfvénically), the normal force is constrained to be *zero* everywhere on the boundary. However, this ceases to be the case as soon as the plasma touches the rigid limiter. Instead, for the sake of self-consistency, the force must be such that a virtual displacement of the plasma into the limiter yields a the force density in the overlap region that matches the limiter force density due to the halo current [15, 18]. Note that the reaction (due to the rigidity of the limiter) to the force per unit area $\xi\, f_\mu$ that the plasma effectively exerts on the limiter is responsible for transforming otherwise *ideally unstable* vertical and kink modes into *resistive modes* which grow either on the L/R time of the limiter/wall or the SOL plasma [18].

Making use of equations (10)–(14), as well as equations (17), (20), (21) and (25), the above matching conditions reduce to

$$\left.\frac{\partial V}{\partial \mu}\right|_{\mu=\mu_\mathrm{p}} = -\mathrm{i}\, n\, h_\mathrm{p}\, \epsilon\, B_\mathrm{o}\, \xi, \tag{91}$$

$$\left.\frac{\partial V'}{\partial \mu}\right|_{\mu=\mu_\mathrm{p}} = \frac{\partial (B_\mathrm{p}\, \xi)}{\partial \nu} - \mathrm{i}\, n\, h_\mathrm{p}\, \epsilon\, B_\mathrm{o}\, \xi, \tag{92}$$

$$B_\mathrm{p} \left.\frac{\partial V'}{\partial \nu}\right|_{\mu=\mu_\mathrm{p}} = -\mathrm{i}\, n\, h_\mathrm{p}\, \epsilon\, B_\mathrm{o}\, (V - V')_{\mu=\mu_\mathrm{p}} + \left(\frac{\kappa\, s^2\, B_\mathrm{p}^2}{h_\mathrm{p}^2} + \kappa\, \beta\, s\, \epsilon\, B_\mathrm{o}^2\, \cos\nu - \mu_0\, a\, h_\mathrm{p}\, f_\mu \right) \xi. \tag{93}$$

5. Nonaxisymmetric VDE model

5.1. Normalization

Let $\hat{x} = x/a$, $\hat{z} = z/a$, $\hat{\beta} = \beta/\epsilon$, $\hat{B}_\mathrm{p} = B_\mathrm{p}/(\epsilon B_\mathrm{o}/s)$, $\hat{\xi} = \xi/(s\,a)$, $\hat{\Xi}^{n=0} = \Xi^{n=0}/a$, $\hat{\Xi}^{n=1} = \Xi^{n=1}/a$, $\hat{V} = V/(a\,\epsilon B_\mathrm{o})$, $\hat{V}' = V'/(a\,\epsilon B_\mathrm{o})$, $\hat{h}_\mathrm{p} = h_\mathrm{p}/s$, $\hat{\delta}_0 = \delta_0/a$, $\hat{\gamma} = \gamma\, \tau_l$, $\hat{I}_{\phi\,\mathrm{p}} = I_{\phi\,\mathrm{p}}/(a\,\epsilon B_\mathrm{o}/\mu_0)$, $\hat{I}_{\theta\,1} = I_{\theta\,1}/(a\,\epsilon B_\mathrm{o}/\mu_0)$, $\hat{I}_{\phi\,\mathrm{s}} = I_{\phi\,\mathrm{s}}/(a\,\epsilon B_\mathrm{o}/\mu_0)$, $\hat{f}_\mu = f_\mu/(\epsilon^2\, B_\mathrm{o}^2/a\,\mu_0)$, $\hat{F}_\mathrm{v} = F_\mathrm{v}/(\epsilon\, B_\mathrm{o}^2\, a^2/\mu_0)$ and $\hat{F}_\mathrm{h} = F_\mathrm{h}/(\epsilon\, B_\mathrm{o}^2\, a^2/\mu_0)$. Here, $\hat{\beta}$ is the normalized toroidal plasma beta, $\hat{B}_\mathrm{p}$ the normalized poloidal magnetic field-strength immediately outside the plasma, $\hat{\xi}$ the normal plasma displacement at the boundary, $\hat{\Xi}^{n=0/n=1}$ the normalized $n = 0/n = 1$ displacement of the plasma centroid relative to that of the vacuum vessel, $\hat{V}$ the normalized perturbed magnetic potential inside the boundary, $\hat{V}'$ the normalized perturbed magnetic potential outside the boundary, $\hat{\delta}_0$ the normalized vacuum vessel radial thickness, $\hat{\gamma}$ the normalized instability growth rate, $\hat{I}_{\phi\,\mathrm{p}}$ the normalized toroidal plasma current, $\hat{I}_{\theta\,1}$ the normalized poloidal halo current (flowing through the limiter), $\hat{I}_{\phi\,\mathrm{s}}$ the normalized toroidal halo current (flowing through the SOL plasma), $\hat{f}_\mu$ the normalized normal halo current force density acting on the vacuum vessel, $\hat{F}_\mathrm{v}$ the normalized net vertical force on the vessel and $\hat{F}_\mathrm{h}$ the normalized net sideways force on the vessel. Recall that τ_l is the L/R time of the vacuum vessel, ϵ the inverse-aspect ratio of the plasma, B_o the on-axis vacuum toroidal magnetic field-strength, a the initial horizontal semi-axis of the plasma, κ the plasma elongation and s a dimensionless scale factor which decreases from 1 to 0 as the VDE progresses.

5.2. Fundamental equations

The plasma equilibrium is determined by the following equations (see section 2):

$$\hat{h}_{\rm p}(\nu) = [1 + (\kappa^2 - 1)\,\cos^2\nu]^{1/2}, \tag{94}$$

$$\hat{B}_{\rm p}(\nu) = \frac{2\,\hat{\beta}^{1/2}}{\alpha}\,[1 - s^3\,\alpha^2\,\sin^2(\nu/2)]^{1/2}, \tag{95}$$

$$q_{\rm p} = \frac{s^2\,\alpha\,Q(\alpha)}{\pi\,\hat{\beta}^{1/2}}, \tag{96}$$

$$Q(\alpha) = \frac{1}{2}\int_0^{\pi}\left[\frac{1 + (\kappa^2 - 1)\,\cos^2\nu}{1 - s^3\,\alpha^2\,\sin^2(\nu/2)}\right]^{1/2} d\nu, \tag{97}$$

$$\hat{I}_{\phi\,\rm p} = 2\int_0^{\pi}\hat{h}_{\rm p}\,\hat{B}_{\rm p}\,{\rm d}\nu, \tag{98}$$

$$c = \frac{\pi/2}{Q(\alpha)\,(1 - s^3\,\alpha^2/2)^{1/2}}. \tag{99}$$

Here, α is an arbitrary constant.

Plasma stability is governed by (see section 4)

$$\hat{V}(\mu,\nu) = \sum_{m\neq 0}[a_m\,\cosh(m\,\mu)\,\cos(m\,[\nu - \pi/2]) + b_m\,\sinh(m\,\mu)\,\sin(m\,[\nu - \pi/2])], \tag{100}$$

$$\hat{V}'(\mu,\nu) = \sum_{m\neq 0} a'_m\,{\rm e}^{-|m|\,(\mu-\mu_{\rm p})}\,{\rm e}^{{\rm i}\,m\,\nu}, \tag{101}$$

$$\left.\frac{\partial\hat{V}}{\partial\mu}\right|_{\mu=\mu_{\rm p}} = -{\rm i}\,n\,s^2\,\hat{h}_{\rm p}\,\hat{\xi}, \tag{102}$$

$$\left.\frac{\partial\hat{V}'}{\partial\mu}\right|_{\mu=\mu_{\rm p}} = \frac{\partial(\hat{B}_{\rm p}\,\hat{\xi})}{\partial\nu} - {\rm i}\,n\,s^2\,\hat{h}_{\rm p}\,\hat{\xi}, \tag{103}$$

$$\hat{B}_{\rm p}\left.\frac{\partial\hat{V}'}{\partial\nu}\right|_{\mu=\mu_{\rm p}} = -{\rm i}\,n\,s^2\,\hat{h}_{\rm p}\,(\hat{V} - \hat{V}')_{\mu=\mu_{\rm p}} + \left(\frac{\kappa\,\hat{B}_{\rm p}^2}{\hat{h}_{\rm p}^2} + \kappa\,\hat{\beta}\,s^3\,\cos\nu - s^3\,\hat{h}_{\rm p}\,\hat{f}_{\mu}\right)\xi, \tag{104}$$

where n is the toroidal mode number, m is a poloidal mode number, a_m, b_m, a'_m are arbitrary constants, and $\mu_{\rm p} = \tanh^{-1}(\kappa^{-1})$.

Finally, the normal halo current force density acting on the vacuum vessel is specified by (see section 3)

$$\hat{f}_{\mu} = \frac{s\,\hat{\gamma}}{2\pi\,c\,q_{\rm p}\,\hat{\delta}_0}\times\left[\frac{f_\phi\,(\mathcal{C}_\theta + [1 - f_\theta]\,\mathcal{C}_\phi) - (1 - f_\theta\,f_\phi)\,\tau\,\mathcal{C}_\phi}{f_\theta\,f_\phi\,(1 - f_\phi) + (1 - f_\theta\,f_\phi)\,\tau}\right]\frac{\hat{B}_{\rm p}}{\hat{B}_{\rm p}(0)}\,\zeta_l, \tag{105}$$

$$\zeta_l(\theta,\phi) = \begin{cases} 1 & \theta_- \leqslant \theta \leqslant \theta_+ \quad\text{and}\quad \phi_- \leqslant \phi \leqslant \phi_+ \\ 0 & \text{otherwise,}\end{cases} \tag{106}$$

$$\mathcal{C}_\theta = \pi[2\,\kappa + p_\kappa\,(\kappa - 1) - p_{\hat{\beta}}\,\kappa\,\beta/2]\frac{s^2}{q_{\rm p}}, \tag{107}$$

$$\mathcal{C}_\phi = \left(p_I\left[\ln\left(\frac{8}{\epsilon\,s}\right) - 2\right] - 1\right)I_{\phi\,\rm p}. \tag{108}$$

Here, f_θ and f_ϕ are, respectively, the poloidal and toroidal angular coverages of the limiter (i.e., the plasma-touching section of the vacuum vessel), whilst τ is the ratio of the L/R time of the vacuum vessel to that of the SOL plasma. The positive constants p_κ and p_I are defined in equations (52) and (57), respectively. Finally,

$$p_{\hat{\beta}} = \frac{{\rm d}\ln\hat{\beta}}{{\rm d}\ln s}. \tag{109}$$

5.3. Derivation of dispersion relation

Let

$$\hat{\xi}(\nu) = \sum_m \xi_m\,{\rm e}^{{\rm i}\,m\,\nu}, \tag{110}$$

where the ξ_m are constants. The first matching condition (102) yields [15, 17]

$$\hat{V}(\mu_{\rm p},\nu) = {\rm i}\sum_{k\neq 0,m'}|k|^{-1}\left[\frac{1 + \lambda^{2|k|}}{1 - \lambda^{2|k|}}\,E_{km'} + \frac{2\,(-\lambda)^{|k|}}{1 - \lambda^{2|k|}}\,E_{-km'}\right]\times{\rm e}^{{\rm i}\,k\,\nu}\,\xi_{m'}, \tag{111}$$

where

$$E_{mm'} = \oint(-n\,s^2\,\hat{h}_{\rm p})\,{\rm e}^{{\rm i}\,(m'-m)\,\nu}\,\frac{{\rm d}\nu}{2\pi}, \tag{112}$$

and

$$\lambda = \frac{\kappa - 1}{\kappa + 1}. \tag{113}$$

Equation (102) also leads to the incompressibility constraint [15, 17]

$$\sum_{m'} E_{0m'}\,\xi_{m'} = 0. \tag{114}$$

The second matching condition (103) implies that [15, 17]

$$\hat{V}'(\mu_{\rm p},\nu) = -{\rm i}\sum_{k\neq 0,m'}|k|^{-1}\,G_{km'}\,{\rm e}^{{\rm i}\,k\,\nu}\,\xi_{m'}, \tag{115}$$

where

$$G_{mm'} = \oint(m\,\hat{B}_{\rm p} - n\,s^2\,\hat{h}_{\rm p})\,{\rm e}^{{\rm i}\,(m'-m)\,\nu}\,\frac{{\rm d}\nu}{2\pi}. \tag{116}$$

Finally, the third matching condition (104), in combination with equations (111) and (115), reduces to the dispersion relation

$$\sum_{m'} F_{mm'}\,\xi_{m'} = 0, \tag{117}$$

where [15, 17]

$$F_{mm'} = \sum_{k\neq 0} G^*_{km}\,|k|^{-1}\,G_{km'} + \sum_{k\neq 0} E^*_{km}\,|k|^{-1}\left[\frac{1 + \lambda^{2|k|}}{1 - \lambda^{2|k|}}\,E_{km'} + \frac{2\,(-\lambda)^{|k|}}{1 - \lambda^{2|k|}}\,E_{-km'}\right] - H_{mm'}, \tag{118}$$

and

$$H_{mm'} = \oint\oint\left(\frac{\kappa\,\hat{B}_{\rm p}^2}{\hat{h}_{\rm p}^2} + \kappa\,\hat{\beta}\,s^3\,\cos\nu - s^3\,\hat{h}_{\rm p}\,\hat{f}_{\mu}\right){\rm e}^{{\rm i}\,(m'-m)\,\nu}\times\frac{{\rm d}\nu}{2\pi}\,\frac{{\rm d}\phi}{2\pi}. \tag{119}$$

Note that, for the sake of simplicity, in deriving the above dispersion relation, we have neglected any coupling of different toroidal harmonics due to toroidal asymmetries in the limiter force distribution.

5.4. Vertical stability

For the $n = 0$ vertical instability, we have

$$G^{n=0}_{mm'} = \frac{1}{\pi}\int_0^\pi m\,\hat{B}_{\rm p}\,\cos[(m'-m)\,\nu]\,{\rm d}\nu, \tag{120}$$

$$H^{n=0}_{mm'} = \frac{\kappa}{\pi}\int_0^\pi \frac{\hat{B}_{\rm p}^2}{\hat{h}_{\rm p}^2}\,\cos[(m'-m)\,\nu]\,{\rm d}\nu + \frac{\kappa\,\hat{\beta}\,s^3}{2}\,(\delta_{m\,m'+1}+\delta_{m\,m'-1}) - \delta H^{n=0}_{mm'}, \tag{121}$$

$$\delta H^{n=0}_{mm'} \simeq \frac{s^3\,\hat{I}_{\phi\,\rm p}\,\Gamma^{n=0}}{2\pi\,c\,q_{\rm p}\,\hat{\delta}_0}\,\mathcal{C}\,{\rm sinc}[(m'-m)\,\pi\,f_\theta/c]\,{\rm e}^{\,{\rm i}\,(m'-m)\,\pi/2}, \tag{122}$$

where

$$\Gamma^{n=0} = \frac{s}{c\,\hat{I}_{\phi\,\rm p}}\,(1-f_\theta) \times\left[\frac{\mathcal{C}_\theta+(1-f_\theta\,f_\phi)\,\mathcal{C}_\phi}{f_\theta\,f_\phi\,(1-f_\phi)+(1-f_\theta\,f_\phi)\,\tau}\right]\hat{\gamma}^{n=0}, \tag{123}$$

$$\mathcal{C} = \frac{f_\theta\,f_\phi}{1-f_\theta}\left[\frac{f_\phi\,(\mathcal{C}_\theta+[1-f_\theta]\,\mathcal{C}_\phi)-(1-f_\theta\,f_\phi)\,\tau\,C_\phi}{\mathcal{C}_\theta+(1-f_\theta\,f_\phi)\,\mathcal{C}_\phi}\right]. \tag{124}$$

Here, $\hat{\gamma}^{n=0}$ is the associated normalized growth rate, and $\Gamma^{n=0}$ a conveniently scaled version of the same. The $n = 0$ force matrix takes the form

$$F^{n=0}_{mm'} = \sum_{k\neq 0} G^{n=0}_{km}\,|k|^{-1}\,G^{n=0}_{km'} - H^{n=0}_{mm'}. \tag{125}$$

Moreover, the incompressibility constraint (114) reduces to $\xi^{n=0}_0 = 0$, and the $n = 0$ dispersion relation becomes

$$\sum_{m'\neq 0} F^{n=0}_{mm'}\,\xi^{n=0}_{m'} = 0 \tag{126}$$

for $m \neq 0$. Finally, the scaled $n = 0$ growth rate is determined by searching for the value of $\Gamma^{n=0}$ which sets the smallest eigenvalue of the $n = 0$ force matrix, (125), to zero.

5.5. Kink stability

For the $n = 1$ kink instability, we have

$$E_{mm'} = \frac{1}{\pi}\int_0^\pi (-s^2\,\hat{h}_{\rm p})\,\cos[(m'-m)\,\nu]\,{\rm d}\nu, \tag{127}$$

$$G^{n=1}_{mm'} = \frac{1}{\pi}\int_0^\pi (m\,\hat{B}_{\rm p}-s^2\,\hat{h}_{\rm p})\,\cos[(m'-m)\,\nu]\,{\rm d}\nu, \tag{128}$$

$$H^{n=1}_{mm'} = \frac{\kappa}{\pi}\int_0^\pi \frac{\hat{B}_{\rm p}^2}{\hat{h}_{\rm p}^2}\,\cos[(m'-m)\,\nu]\,{\rm d}\nu + \frac{\kappa\,\hat{\beta}\,s^3}{2}\,(\delta_{m\,m'+1}+\delta_{m\,m'-1}) - \delta H^{n=1}_{mm'}, \tag{129}$$

$$\delta H^{n=1}_{mm'} \simeq \frac{s^3\,\hat{I}_{\phi\,\rm p}\,\Gamma^{n=1}}{2\pi\,c\,q_{\rm p}\,\hat{\delta}_0}\,\mathcal{C}\,{\rm sinc}[(m'-m)\,\pi\,f_\theta/c]\,{\rm e}^{\,{\rm i}\,(m'-m)\,\pi/2}, \tag{130}$$

where

$$\Gamma^{n=1} = \frac{s}{c\,\hat{I}_{\phi\,\rm p}}\,(1-f_\theta) \times\left[\frac{\mathcal{C}_\theta+(1-f_\theta\,f_\phi)\,\mathcal{C}_\phi}{f_\theta\,f_\phi\,(1-f_\phi)+(1-f_\theta\,f_\phi)\,\tau}\right]\hat{\gamma}^{n=1}. \tag{131}$$

Here, $\hat{\gamma}^{n=1}$ is the associated normalized growth rate, and $\Gamma^{n=1}$ a conveniently scaled version of the same. The $n = 1$ force matrix takes the form

$$F^{n=1}_{mm'} = \sum_{k\neq 0} G^{n=1}_{km}\,|k|^{-1}\,G^{n=1}_{km'} + \sum_{k\neq 0} E_{km}\,|k|^{-1}\left[\frac{1+\lambda^{2|k|}}{1-\lambda^{2|k|}}\,E_{km'}+\frac{2\,(-\lambda)^{|k|}}{1-\lambda^{2|k|}}\,E_{-km'}\right] - H^{n=1}_{mm'}. \tag{132}$$

However, the $n = 1$ dispersion relation,

$$\sum_{m'} F^{n=1}_{mm'}\,\xi^{n=1}_{m'} = 0, \tag{133}$$

must be solved subject to the incompressibility constraint

$$\sum_{m'} E_{0m'}\,\xi^{n=1}_{m'} = 0. \tag{134}$$

This is equivalent to solving the unconstrained dispersion relation [17]

$$\sum_{m'} \tilde{F}^{n=1}_{mm'}\,\tilde{\xi}^{n=1}_{m'} = 0, \tag{135}$$

where

$$\tilde{F}^{n=1}_{mm'} = \sum_{k,l} P_{mk}\,F^{n=1}_{kl}\,P_{lm'}, \tag{136}$$

$$\xi^{n=1}_m = \sum_{m'} P_{mm'}\,\tilde{\xi}^{n=1}_{m'}, \tag{137}$$

and

$$P_{mm'} = \delta_{m\,m'} - \frac{E_{0m}\,E_{0m'}}{\sum_k (E_{0k})^2}. \tag{138}$$

Thus, the scaled $n = 1$ growth rate is determined by searching for the value of $\Gamma^{n=1}$ which sets the smallest eigenvalue of the transformed $n = 1$ force matrix, (136), to zero.

5.6. Determination of limiter boundaries

The parametric equation of the LCFS (in the poloidal plane) is written (see equations (6) and (7))

$$\hat{x} = s\,\cos\nu, \tag{139}$$

$$\hat{z} = \kappa\,s\,\sin\nu. \tag{140}$$

For the sake of simplicity, the inner surface of the vacuum vessel is assumed to coincide with the LCFS when $s = 1$. Thus, the parametric equation of the inner surface of the vacuum vessel (in a coordinate system whose origin is coincident with the plasma centroid in the poloidal plane) takes the form

$$\hat{x}' = \cos\nu', \tag{141}$$

$$\hat{z}' = \kappa_0\,\sin\nu' - \hat{\Xi}^{n=0} - \hat{\Xi}^{n=1}\,\cos\phi, \tag{142}$$

where $\kappa_0 \equiv \kappa(s = 1)$, $\hat{\Xi}^{n=0}$ is the $n = 0$ displacement of the plasma centroid relative to that of the vacuum vessel (normalized to a), and $\hat{\Xi}^{n=1}\cos\phi$ is the corresponding $n = 1$ displacement. (Here, for the sake of simplicity, we are neglecting any helical variation of the $n = 1$ displacement.) The constraint

$$\hat{\Xi}^{n=0} + \hat{\Xi}^{n=1} = \kappa_0 - \kappa\,s \tag{143}$$

ensures that the LCFS remains in contact with the inner boundary of the vacuum vessel at the geometric centre of the limiter (i.e. at $\nu = \nu' = \pi/2$ and $\phi = 0$).

Since $d(\hat{\Xi}^{n=0} + \hat{\Xi}^{n=1})/ds = -[\kappa + p_\kappa\,(\kappa - 1)]$, according to equations (52) and (143), let us assume that

$$\frac{d\hat{\Xi}^{n=0}}{ds} = \begin{cases} -\left(\dfrac{\Gamma^{n=0}}{\Gamma^{n=0}+\Gamma^{n=1}}\right)[\kappa + p_\kappa\,(\kappa-1)] \\ \quad \Gamma^{n=1} > 0, \quad \Gamma^{n=0} > 0 \\ -[\kappa + p_\kappa\,(\kappa-1)] \\ \quad \Gamma^{n=1} \leqslant 0, \quad \Gamma^{n=0} > 0, \end{cases} \tag{144}$$

and

$$\frac{d\hat{\Xi}^{n=1}}{ds} = \begin{cases} -\left(\dfrac{\Gamma^{n=1}}{\Gamma^{n=0}+\Gamma^{n=1}}\right)[\kappa + p_\kappa\,(\kappa-1)] \\ \quad \Gamma^{n=1} > 0, \quad \Gamma^{n=0} > 0 \\ 0 \\ \quad \Gamma^{n=1} \leqslant 0, \quad \Gamma^{n=0} > 0. \end{cases} \tag{145}$$

According to this assumption, when the $n = 0$ vertical and $n = 1$ kink instabilities are both unstable, the ratio of the derivatives of the $n = 0$ and $n = 1$ plasma displacements with respect to the plasma shrinkage factor, s, is equal to the ratio of the instantaneous linear growth rates of the corresponding instabilities. This is reasonable because $1 - s$ plays the role of an effective time during the VDE. The initial conditions for the previous two equations are $\hat{\Xi}^{n=0}(s = 1) = 0$, and

$$\hat{\Xi}^{n=1}(s = 1) = 0, \tag{146}$$

respectively.

In the vicinity of the limiter, the parametric equation of the outer boundary of the halo is approximately

$$\hat{x}'' = s\,\cos\nu, \tag{147}$$

$$\hat{z}'' = \kappa\, s\,\sin\nu + \hat{\delta}_0, \tag{148}$$

where $\hat{\delta}_0 \ll 1$ is the local halo thickness (which is the same as the local thickness of the vacuum vessel) normalized to a. The angular boundary of the limiter is determined by the simultaneous solution of $\hat{x}' = \hat{x}''$ and $\hat{z}' = \hat{z}''$: i.e. it corresponds to the locus of those points at which the outer boundary of the halo is coincident with the inner boundary of the vacuum vessel.

Let us calculate the poloidal extent of the limiter at $\phi = 0$. This is specified by $s\cos\nu = \cos\nu'$ (i.e. $\hat{x}'' = \hat{x}'$) and $\kappa\, s\,\sin\nu = \kappa_0\,\sin\nu' - \Xi$ (i.e. $\hat{z}'' = \hat{z}'(\phi = 0)$), where

$$\Xi \equiv \hat{\Xi}^{n=0} + \hat{\Xi}^{n=1} + \hat{\delta}_0 = \kappa_0 - \kappa\, s + \hat{\delta}_0. \tag{149}$$

Moreover, given that $\theta \simeq c\,(\nu - \pi/2)$ (see equation (31)), the limiter boundaries are located at $\nu_\pm \simeq \pi/2 \pm \pi\, f_\theta/c$ (see figure 1). Hence, $\cos\nu_\pm = \mp\sin(\pi\, f_\theta/c)$ and $\sin\nu_\pm = \cos(\pi\, f_\theta/c)$. Finally,

$$s^2\,\cos^2\nu_\pm = 1 - \left(\frac{\kappa\, s\,\sin\nu_\pm + \Xi}{\kappa_0}\right)^2, \tag{150}$$

which yields

$$\cos(\pi\, f_\theta/c) = \frac{\kappa\,\Xi - \sqrt{\kappa^2\,\Xi^2 - (\kappa_0^2 - \kappa^2)\,[(1-s^2)\,\kappa_0^2 - \Xi^2]}}{(\kappa_0^2 - \kappa^2)\,s}. \tag{151}$$

Let us calculate the toroidal extent of the limiter at $\nu = \nu' = \pi/2$. This is specified by $\kappa\, s = \kappa_0 - \Xi - \hat{\Xi}^{n=1}\,(\cos\phi - 1)$ (i.e. $\hat{z}''(\nu = \pi/2) = \hat{z}'(\nu' = \pi/2)$), which reduces to $\sin^2(\phi/2) = \hat{\delta}_0/(2\,\hat{\Xi}^{n=1})$. (Note that $\hat{x}''(\nu = \pi/2) = \hat{x}'(\nu' = \pi/2)$ is automatically satisfied.) Now, the limiter boundaries are located at $\phi_\pm = \pm\pi\, f_\phi$ (see figure 1). It follows that

$$\sin(\pi\, f_\phi/2) = \begin{cases} 1 & \hat{\Xi}^{n=1} \leqslant \hat{\delta}_0/2 \\ 1/[\hat{\delta}_0/(2\,\hat{\Xi}^{n=1})]^{1/2} & \hat{\Xi}^{n=1} > \hat{\delta}_0/2. \end{cases} \tag{152}$$

Equations (145), (146), (151) and (152) effectively determine the poloidal and toroidal angular extents of the limiter, f_θ and f_ϕ, respectively, as functions of the scale factor, s.

5.7. VDE simulations

Our VDE simulations consist of two main phases. In the so-called *shrinkage phase*, which corresponds to $1 \geqslant s \geqslant s_c$,

$$\kappa = 1 + (\kappa_0 - 1)\, s^{\,p_\kappa}, \tag{153}$$

$$\hat{\beta} = \hat{\beta}_0\, s^{\,p_{\hat{\beta}}}, \tag{154}$$

$$\hat{I}_{\phi\,\mathrm{p}} = \hat{I}_{\phi\,\mathrm{p}\,0}\, s^{\,p_I}, \tag{155}$$

where κ_0, $\hat{\beta}_0$, and $\hat{I}_{\phi\,\mathrm{p}\,0}$ are the initial plasma elongation, normalized plasma beta and normalized plasma current, respectively, and p_κ, $p_{\hat{\beta}}$ and p_I are positive constants (see equations (52), (109), and (57)). On the other hand, in the so-called *quench phase*, which corresponds to $s_c > s$,

$$\kappa = 1 + (\kappa_0 - 1)\, s^{\,p_\kappa}, \tag{156}$$

$$\hat{\beta} = \hat{\beta}_0\, s_c^{\,p_{\hat{\beta}} - p'_{\hat{\beta}}}\, s^{\,p'_{\hat{\beta}}}, \tag{157}$$

$$\hat{I}_{\phi\,\mathrm{p}} = \hat{I}_{\phi\,\mathrm{p}\,0}\, s_c^{\,p_I - p'_I}\, s^{\,p'_I} \tag{158}$$

where $p'_{\hat{\beta}} > p_{\hat{\beta}}$ and $p'_I > p_I$. Incidentally, it is generally convenient to specify the initial edge safety factor, $q_{p\,0}$, rather than the normalized initial plasma current, $\hat{I}_{\phi\,\mathrm{p}\,0}$ (see equations (94)–(98)).

It is helpful to define the composite scaled growth rate

$$\Gamma = \begin{cases} \Gamma^{n=0} + \Gamma^{n=1} & \Gamma^{n=1} > 0, \quad \Gamma^{n=0} > 0 \\ \Gamma^{n=0} & \Gamma^{n=1} \leqslant 0, \quad \Gamma^{n=0} > 0. \end{cases} \tag{159}$$

The poloidal halo current, including currents driven by both $n = 0$ and $n = 1$ instabilities, and expressed as a fraction of the original toroidal plasma current, becomes (see equation (67))

$$\mathcal{I}_\theta \equiv \frac{\hat{I}_{\theta\,1}}{\hat{I}_{\phi\,\mathrm{p}\,0}} = \frac{\hat{I}_{\phi\,\mathrm{p}}}{\hat{I}_{\phi\,\mathrm{p}\,0}}\,\frac{f_\phi\,\Gamma}{q_\mathrm{p}\,(1 - f_\theta)}, \tag{160}$$

whereas toroidal peaking factor for the halo current is written (see equation (68))

$$\mathcal{I}_\phi = \frac{1}{f_\phi}. \tag{161}$$

The toroidal SOL current, expressed as a fraction of the toroidal plasma current, takes the form (see equation (70))

$$\mathcal{I}_\phi \equiv \frac{\hat{I}_{\phi\,\mathrm{s}}}{\hat{I}_{\phi\,\mathrm{p}}} = \Gamma. \tag{162}$$

Furthermore, the normalized net vertical force acting on the vacuum vessel is written (see equation (79))

$$\hat{F}_{\rm v} \simeq \frac{2\pi\, s\, \hat{I}_{\phi\,\rm p}\, \Gamma}{c\, q_{\rm p}}\, \mathcal{C}\, \mathrm{sinc}(\pi\ f_\theta/c), \tag{163}$$

and the normalized net sideways force becomes (see equation (81))

$$\hat{F}_{\rm h} \simeq \frac{2\pi^2\, \kappa\, s\, \hat{I}_{\phi\,\rm p}\, \Gamma}{c^2\, q_{\rm p}}\, f_\theta\, \mathcal{C}\, \mathrm{sinc}^2(\pi\ f_\theta/c)\, \mathrm{sinc}(\pi\ f_\phi). \tag{164}$$

It is hypothesized that the quench phase is triggered as soon as the toroidal SOL current fraction, $\mathcal{I}_\phi$, exceeds some critical value $\Gamma_{\rm c}$, where $0 < \Gamma_{\rm c} < 1$: i.e. as soon as the scaled composite growth rate Γ exceeds $\Gamma_{\rm c}$ (see equation (162)). The reasoning behind this hypothesis is that, as the VDE develops, more and more toroidal current is transferred inductively from the relatively hot main plasma to the relatively cold SOL plasma. However, there is a limit to how far this transfer can proceed. For instance, it would not make any sense for the current flowing in the SOL plasma to exceed the original current flowing in the main plasma, which implies that the transfer must stop before Γ exceeds unity. Thus, in our model, the quench phase effectively prevents the toroidal current flowing in the SOL plasma from becoming unphysicaly large. Note, however, that the above hypothesis is consistent with the experimental observation that the quench is triggered by low values of the edge safety factor. This follows because, once $q_{\rm p}$ has fallen to a small enough value to destabilize the $n = 1$ kink mode, the normalized growth rate of this mode, $\Gamma^{n=1}$, tends to increase very rapidly with any further decrease in $q_{\rm p}$ (unlike $\Gamma^{n=0}$, which exhibits weak variation with $q_{\rm p}$), and the quench criterion $\Gamma \equiv \Gamma^{n=0} + \Gamma^{n=1} > \Gamma_{\rm c}$ is soon satisfied. The above hypothesis is also consistent with the idea that the quench is ultimately caused by the development of *magnetic ergodicity* within the plasma [21–23]. This follows because the degree of ergodicity of the magnetic field inside the plasma is a highly nonlinear function of the amplitude of the nonaxisymmetric $n = 1$ kink mode, and, according to the above discussion, the quench criterion $\Gamma > \Gamma_{\rm c}$ is only likely to be satisfied when this amplitude has attained a significant value.

5.8. Summary of model

The nonaxisymmetric VDE model described in this paper is rather involved, since it incorporates stability calculations for the vertical and kink modes, circuital equations for the halo currents, and a shrinkage model for the plasma shape, pressure and current. For the sake of clarity, the complete model is summarized below.

The *free parameters* in the model are as follows. (i) ϵ—the initial inverse aspect-ratio. (ii) κ_0—the initial vertical elongation. (iii) $\hat{\beta}_0$—the initial toroidal plasma beta (normalized to the initial inverse aspect-ratio, ϵ). (iv) $q_{\rm p\,0}$—the initial edge safety factor. (v) $\hat{\delta}_0$—the mean radial thickness of the vacuum vessel (normalized to the initial horizontal semi-axis of the plasma, a). (vi) τ—the ratio of the vacuum vessel time-constant to that of the SOL plasma. (vii) $\Gamma_{\rm c}$—the critical toroidal halo current fraction at which the quench phase is triggered. (viii) p_κ, $p_{\hat{\beta}}$, p_I, $p_{\hat{\beta}'}$, p'_I—various dimensionless parameters which govern the variation of the plasma elongation, normalized beta and normalized toroidal current during the shrinkage and quench phases. Note that the parameter $q_{\rm p\,0}$ is converted into the equivalent parameter $\hat{I}_{\phi\,\rm p\,0}$—the normalized initial toroidal plasma current—with the aid of equations (94)–(98) (with $s = 1$, $\kappa = \kappa_0$, $\hat{\beta} = \hat{\beta}_0$, and the parameter α adjusted until $q_{\rm p} = q_{p\,0}$.)

During the *shrinkage phase*, the plasma shrinkage factor s gradually decreased from unity. The normalized $n = 1$ plasma displacement is given the initial value $\hat{\Xi}^{n=1} = 0$. At each s value, the following calculation is performed. (i) The elongation, κ, normalized plasma beta, $\hat{\beta}$, and normalized toroidal plasma current, $\hat{I}_{\phi\,\rm p}$, are calculated from equations (153)–(155), respectively. The edge safety factor is then determined from equations (94)–(99) (by adjusting α until the correct $\hat{I}_{\phi\,\rm p}$ is obtained). (ii) The poloidal and toroidal induction parameters $\mathcal{C}_\theta$ and $\mathcal{C}_\phi$ are determined from equations (107) and (108), respectively. (iii) The normalized net plasma displacement Ξ is determined from equation (149). (iv) The fractional poloidal and toroidal coverages of the limiter are determined from equations (151) and (152), respectively. (v) The elements of the $n = 0$ F-matrix are determined from equations (113) and (120)–(125). (vi) The $n = 0$ matrix eigenvalue problem is solved to determine the normalized $n = 0$ growth rate, $\Gamma^{n=0}$. (vii) The elements of the $n = 1$ F-matrix are determined from equations (127)–(132). (viii) The $n = 1$ matrix eigenvalue problem is solved to determine the normalized $n = 1$ growth rate, $\Gamma^{n=1}$. (ix) Equation (145) is integrated to give the new value of the normalized $n = 1$ plasma displacement, $\hat{\Xi}^{n=1}$. (x) The parameters $\mathcal{I}_\theta$, $\mathcal{T}_\phi$, $\mathcal{I}_\phi$, $\hat{F}_{\rm v}$ and $\hat{F}_\phi$ are determined from equations (159)–(160), (161), (162), (163) and (164), respectively.

The *quench phase* is triggered once $\Gamma \equiv \Gamma^{n=0} + \Gamma^{n=1}$ exceeds the critical value $\Gamma_{\rm c}$ (at, $s = s_{\rm c}$, say). During the quench phase, the shrinkage factor s gradually decreased from $s_{\rm c}$. At each s value, the following calculation is performed. (i) The elongation, κ, normalized plasma beta, $\hat{\beta}$, and normalized toroidal current, $\hat{I}_{\phi\,\rm p}$, are calculated from equations (156)–(158), respectively. (ii)–(x) The remaining steps in the calculation are the same as in the shrinkage phase.

6. Results

6.1. Example VDE simulation

Figures 4–9 show data from an example VDE simulation performed with the following parameters: $\epsilon = 0.3$, $\kappa_0 = 1.5$, $\hat{\beta}_0 = 0.15$, $q_{\rm p\,0} = 4.0$, $\tau = 0.01$, $\hat{\delta}_0 = 0.05$, $p_\kappa = 0.$, $p_{\hat{\beta}} = 0.$, $p_I = 0.2$, $p'_{\hat{\beta}} = 100.0$, $p'_I = 5.0$, $\Gamma_{\rm c} = 0.5$. The fact that τ, which is the ratio of the resistivity of the SOL plasma to that of the limiter, is small compared with unity indicates that the limiter is much more resistive than the SOL plasma. Moreover, setting $\Gamma_{\rm c} = 0.5$ means that the quench phase (in which the plasma current and pressure both decay rapidly in time) is triggered as soon as the toroidal current flowing in the SOL plasma exceeds 50% of the net toroidal plasma current. The fact that $p'_{\hat{\beta}} \gg p'_I$ implies that the thermal quench is much more rapid than the current quench, in accordance with experimental observations.

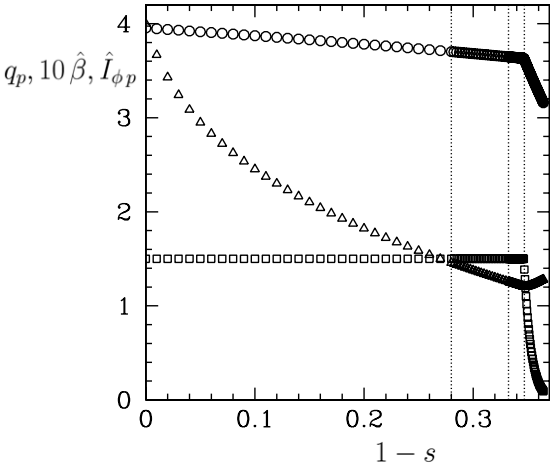

Figure 4. Example VDE simulation. Edge safety factor, $q_{\rm p}$ (triangles), $10\times$ normalized plasma beta, $10\,\hat{\beta}$ (squares), and normalized toroidal plasma current, $\hat{I}_{\phi\,\rm p}$ (circles), versus cross-section shrinkage factor, $1-s$. Simulation parameters: $\epsilon = 0.3$, $\kappa_0 = 1.5$, $\hat{\beta}_0 = 0.15$, $q_{\rm p\,0} = 4.0$, $\tau = 0.01$, $\hat{\delta}_0 = 0.05$, $p_\kappa = 0.$, $p_{\hat{\beta}} = 0.$, $p_I = 0.2$, $p'_{\hat{\beta}} = 100.0$, $p'_I = 5.0$, $\Gamma_{\rm c} = 0.5$. Vertical dotted lines indicate onset of kink instability, onset of toroidal localization of limiter, and onset of quench phase, in order from left to right.

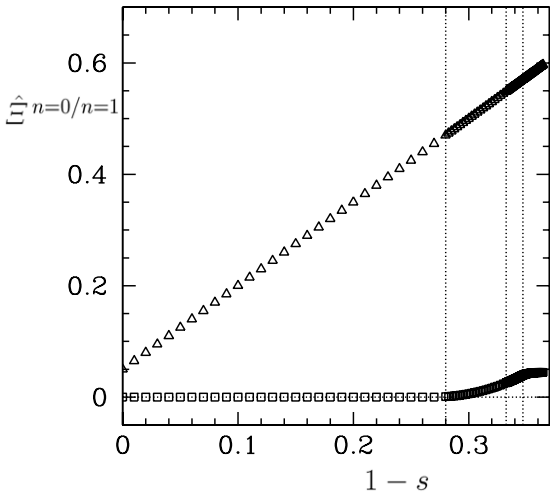

Figure 5. Example VDE simulation. Normalized amplitude of $n = 0/n = 1$ displacement of plasma poloidal centroid, $\hat{\Xi}^{n=0/n=1}$ (triangles/squares), versus cross-section shrinkage factor, $1-s$. See figure 4 caption.

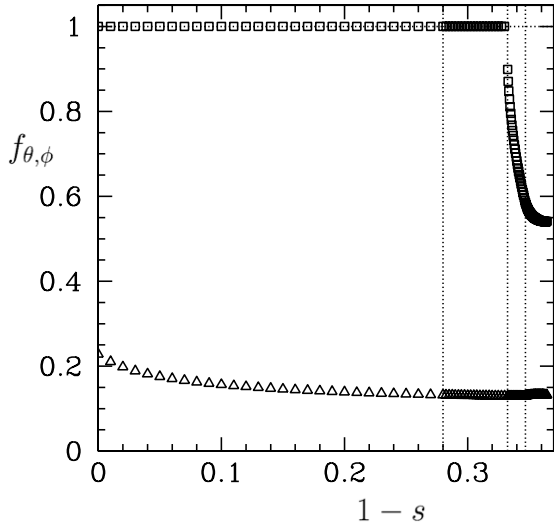

Figure 6. Example VDE simulation. Poloidal/toroidal fractional coverage of limiter, $f_{\theta,\phi}$ (triangles/squares), versus cross-section shrinkage factor, $1-s$. See figure 4 caption.

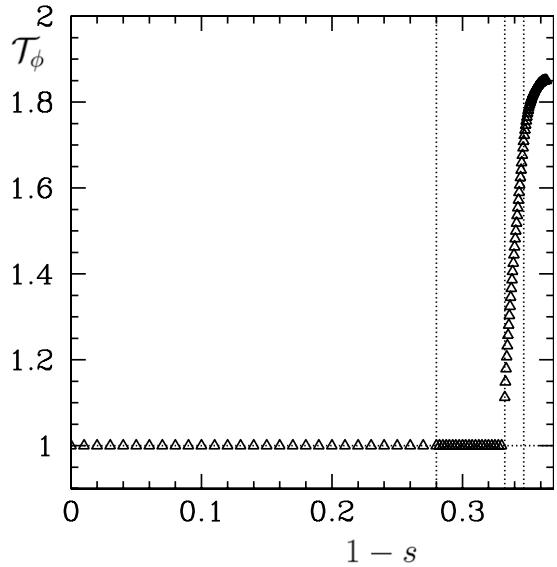

Figure 7. Example VDE simulation. Toroidal peaking factor for poloidal halo current, $\mathcal{T}_\phi$, versus cross-section shrinkage factor, $1-s$. See figure 4 caption.

It can be seen, from figures 4–9, that in the so-called *shrinkage phase*—during which the cross-sectional area of the main plasma shrinks, as it interacts with the vacuum vessel, at constant plasma beta, constant plasma elongation, and (almost) constant plasma current, and the edge safety factor consequently *decreases* in time—the $n = 1$ kink instability is initially *stable*. (On the other hand, the $n = 0$ vertical instability is unstable throughout the whole simulation. Incidentally, the degree of plasma shrinkage is parametrized by $1-s$, which also acts as an effective time, measured from the onset of the VDE.) However, it can also be seen that when the plasma has shrunk sufficiently that its edge safety factor falls below some critical value, lying between 1 and 2, the $n = 1$ kink mode becomes *unstable*. Initially, the amplitude of the kink mode is not large enough to cause toroidal localization of the limiter (i.e. $\hat{\Xi}^{n=1} < \hat{\delta}_0/2$—see equation (152)), implying that the poloidal halo current distribution remains *toroidally symmetric*. Later, however, the kink mode amplitude grows sufficiently large to cause localization of the limiter, and the halo current distribution consequently becomes *toroidally asymmetric*. Finally, the so-called *quench phase* commences when the toroidal halo current fraction exceeds a critical value. In this phase, the plasma current and pressure both decay in time, although the pressure decays much more rapidly than the current. The edge safety factor *increases* during the quench phase because the current decays more rapidly than the cross-sectional area of the plasma shrinks.

It follows, from the above discussion, that a typical VDE consists of *four* identifiable stages. Stage I (to the left of

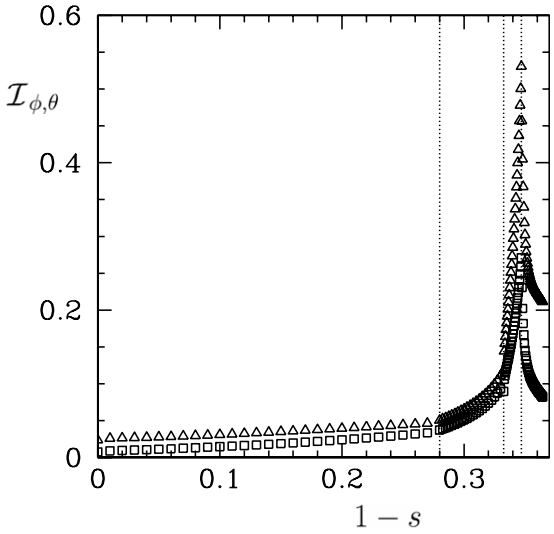

Figure 8. Example VDE simulation. Toroidal/poloidal halo current fraction, $\mathcal{I}_{\phi,\theta}$ (triangles/squares), versus cross-section shrinkage factor, $1-s$. See figure 4 caption.

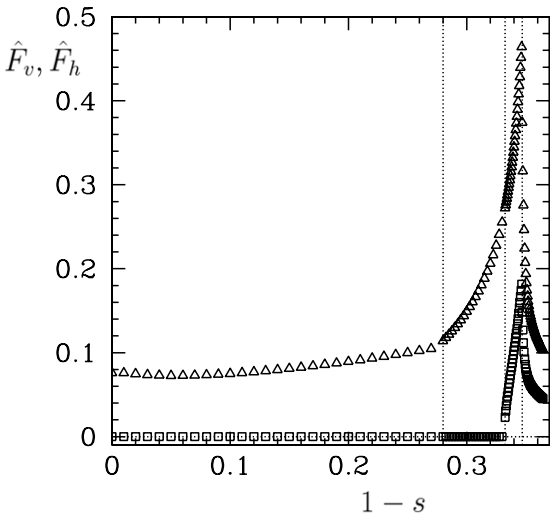

Figure 9. Example VDE simulation. Normalized net vertical/sideways force acting on vacuum vessel, $\hat{F}_{\rm v,h}$ (triangles/squares), versus cross-section shrinkage factor, $1-s$. See figure 4 caption.

the first vertical dotted line in figures 4–9) corresponds to the initial part of the shrinkage phase in which the $n=1$ kink mode is *stable*. Stage II (between the first and second vertical dotted lines) corresponds to the intermediate part of the shrinkage phase in which the $n=1$ kink mode is *unstable*, but the halo current distribution is *toroidally symmetric*. Stage III (between the second and the third vertical dotted lines) corresponds to the final part of the shrinkage phase in which the growing kink mode renders the halo current distribution *toroidally asymmetric*. Finally, stage IV (to the right of the third vertical dotted line) corresponds to the *quench phase*.

Figures 8 and 9 indicate that the toroidal and poloidal halo current fractions, as well as the normalized net vertical force acting on the vacuum vessel, are comparatively small during stage I of the VDE: i.e. when the kink mode is stable. However, the onset of kink mode instability, at the start of stage II, instigates a rapid increase in the halo current fractions and the vertical force. Moreover, during stage III, when the kink mode amplitude is sufficiently large to produce toroidal asymmetry of the halo current distribution, the halo current fractions and vertical force start to increase even faster. Finally, in the quench phase, which corresponds to stage IV, the halo current fractions and vertical force decay rapidly. Consequently, the peak halo current fraction, the peak vertical force, and the minimum edge safety factor, all occur at the onset of the current and pressure quench—i.e. at the start of stage IV of the VDE. Figures 8 and 9 also show that the net sideways force acting on the vacuum vessel is zero (by symmetry) in stages I and II, becomes non-zero and grows rapidly in stage III, and then decays rapidly in stage IV. Moreover, the peak sideways force is a significant fraction of the peak vertical force.

Recall that, for the sake of simplicity, our model neglects the effect of current gradients on the stability of the $n=1$ kink mode. This is a reasonable approximation during the shrinkage phase of a VDE. However, strong current gradients are likely to be generated within the plasma during the quench phase, because the current in the outermost regions of the plasma almost certainly decays faster than that in the core. It follows that our model probably significantly underestimates the growth rate of the $n=1$ kink mode during the quench phase. This may explain why the model predicts that the halo current fraction and the forces on the vacuum vessel peak at the start of the quench phase, rather than during this phase, as is generally the case in experiments.

For typical ITER parameters (i.e. $\epsilon=0.34$, $B_{\rm o}=5.68\,{\rm T}$ and $a=2.8\,{\rm m}$ [14]) the peak vertical and horizontal forces on the vacuum vessel inferred from the example simulation are 31 MN and 12 MN, respectively.

6.2. *VDE parameter scans*

In the following, all plotted values (except $\hat{\mathcal{I}}_{\phi\,{\rm p}\,0}$ and $\hat{\beta}_0$) are evaluated at the start of the quench phase, when the halo current and halo current force achieve their maximum values, and the edge safety factor reaches its minimum value.

Figures 10–13 display data from a collection of VDE simulations performed with a wide range of different values of the parameters $\hat{\beta}_0$, $q_{p\,0}$, κ_0 and τ. Note that the range of $\hat{\beta}$ values used in these simulations spans all cases in which the kink mode is stable when $q_{\rm p}=q_{\rm p\,0}$. Figure 10 shows the toroidal peaking factor for the poloidal halo current, $\mathcal{T}_\phi$, versus the poloidal halo current fraction, $\mathcal{I}_\theta$. The plot exhibits the characteristic *inverse* relationship between $\mathcal{T}_\phi$ and $\mathcal{I}_\theta$ that has been observed experimentally on many different tokamaks [7–9]. Moreover, the actual values of $\mathcal{T}_\phi$ and $\mathcal{I}_\theta$ are very much in line with those seen in experiments [7–9]. Figure 11 shows $\mathcal{I}_\theta\,\mathcal{T}_\phi$, which is a measure of the *peak poloidal halo current density* in the vacuum vessel, versus the effective edge safety factor for class-2 halo current filaments, $q_{p\,2}$ (see equation (42)). (Recall that class-2 filaments are responsible for the halo current force acting on the vessel.) It can be seen that there is a strong *inverse* relationship between the peak halo current density and the minimum effective safety factor. Figure 12 shows the ratio of the normalized net sideways force, $\hat{F}_{\rm h}$, acting on the vacuum vessel, to the normalized net vertical

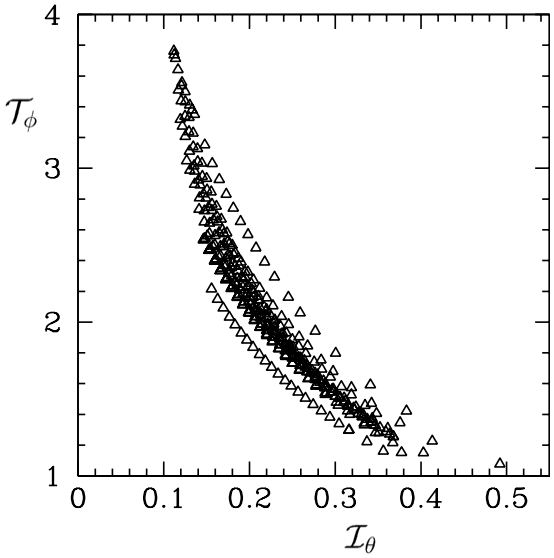

Figure 10. VDE parameter scan. Toroidal peaking factor for poloidal halo current, $\mathcal{T}_\phi$, versus poloidal halo current fraction, $\mathcal{I}_\theta$, for VDE simulations performed with $\hat{\beta}_0$ in the range 0.0–0.35, $q_{\rm p0}$ in the range 2.0–5.0, κ_0 in the range 1.1–1.7, and τ in the range 0.01–1.0. The other simulation parameters are $\epsilon = 0.3$, $\hat{\delta}_0 = 0.05$, $p_\kappa = 0.$, $p_{\hat{\beta}} = 0.$, $p_I = 0.2$, $p'_{\hat{\beta}} = 100.0$, $p'_I = 5.0$, $\Gamma_{\rm c} = 0.5$.

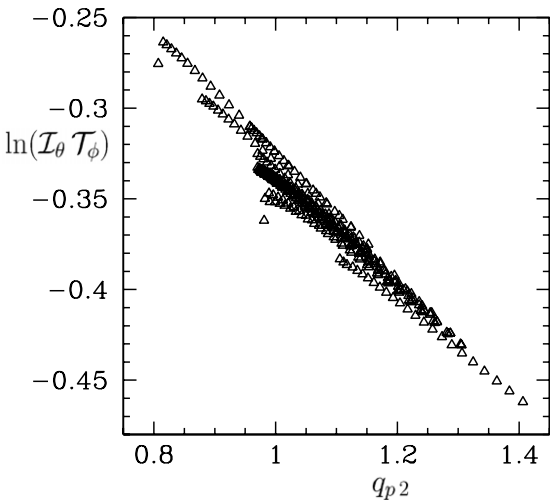

Figure 11. VDE parameter scan. Peak poloidal halo current density parameter, $\mathcal{I}_\theta\,\mathcal{T}_\phi$, versus minimum effective edge safety factor, $q_{\rm p2}$, for VDE simulations shown in figure 10.

force, $\hat{F}_{\rm v}$, versus the normalized initial plasma beta, $\hat{\beta}_0$. There is a clear correlation between the plasma beta and the ratio of the sideways force to the vertical force. Moreover, the ratio approaches unity at comparatively high-beta values. Finally, figure 13 shows $\hat{F}_{\rm v}\,\mathcal{T}_\phi$, which is a measure of the normalized *peak vertical force density* in the vacuum vessel, versus the normalized initial toroidal plasma current, $\hat{I}_{\phi\,{\rm p}0}$. It can be seen that increasing $\hat{F}_{\rm v}\,\mathcal{T}_\phi$ correlates strongly with increasing $\hat{I}_{\phi\,{\rm p}0}$. However, the plot also exhibits a strong correlation between increasing vacuum vessel resistivity, relative to the SOL plasma, and increasing force density: i.e. between decreasing τ and increasing $\hat{F}_{\rm v}\,\mathcal{T}_\phi$ [21–23].

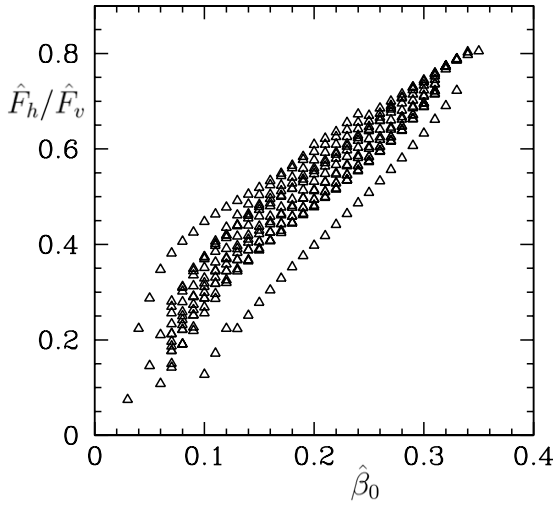

Figure 12. VDE parameter scan. Ratio of normalized net sideways force acting on vacuum vessel, $\hat{F}_{\rm h}$, to normalized net vertical force, $\hat{F}_{\rm v}$, versus normalized initial plasma beta, $\hat{\beta}_0$, for VDE simulations shown in figure 10.

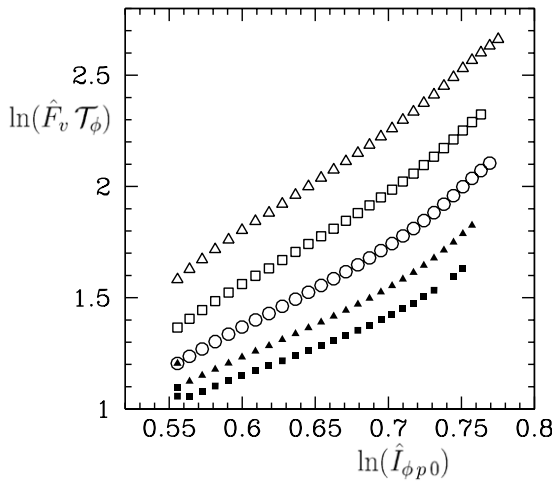

Figure 13. VDE parameter scan. Normalized peak vertical force density parameter, $\hat{F}_{\rm v}\,\mathcal{T}_\phi$, versus normalized initial toroidal plasma current, $\hat{I}_{\phi\,{\rm p}0}$, for VDE simulations performed with a range of different $\hat{\beta}_0$ and τ values. The other simulation parameters are $\epsilon = 0.3$, $\kappa_0 = 1.5$, $q_{\rm p0} = 3.0$, $\hat{\delta}_0 = 0.05$, $p_\kappa = 0.$, $p_{\hat{\beta}} = 0.$, $p_I = 0.2$, $p'_{\hat{\beta}} = 100.0$, $p'_I = 5.0$, and $\Gamma_{\rm c} = 0.5$. The open triangles, open squares, open circles, filled triangles and filled squares correspond to $\tau = 0.0625$, 0.125, 0.25, 0.5 and 1.0, respectively.

7. Summary

We have developed an essentially *analytic* model of a nonaxisymmetric VDE in a vertically elongated tokamak plasma. The model employs a large aspect-ratio, high-beta (i.e. $\beta \sim \epsilon$), *sharp-boundary* plasma equilibrium (see section 2) in which the perturbed edge pressure balance is modified in response to the halo current force exerted on the section of the vacuum vessel that is in direct electrical contact with the main plasma (see section 4). Moreover, the angular boundaries of this plasma-touching section are determined self-consistently from the calculated amplitudes of the $n = 0$ and the $n = 1$ plasma displacements (see section 5.6). Finally,

the halo current is determined from circuit analysis using driving inductive voltages obtained from the calculated linear growth rates of the $n = 0$ and the $n = 1$ modes (see section 3).

We have used our model to simulate nonaxisymmetric VDEs with a wide range of different plasma equilibrium and vacuum vessel parameters (see section 6). These simulations yield toroidal peaking factors and poloidal halo current fractions whose magnitudes are similar to those observed experimentally [7–9], and also reproduce the characteristic inverse scaling between the peaking factor and halo current fraction [7–9]. In addition, the peak halo current density in the vacuum vessel is found to vary as the reciprocal of the minimum edge safety factor reached during the VDE. Moreover, under certain circumstances, the net sideways acting force acting on the vessel, expressed as a fraction of the net vertical force, is observed to approach unity. Finally, the peak vertical force density in the vacuum vessel correlates strongly with the toroidal plasma current at the onset of the VDE, but also increases with increasing vacuum vessel resistivity relative to the SOL plasma. Some of the results of our simulations—in particular, the findings that the vessel forces are larger for more unstable plasmas, and generally increase with increasing vessel resistivity—are consistent with those recently obtained by Paccagnella, Strauss *et al* [21–23].

Note that our model depends crucially on the assumption that the normal plasma velocity is *non-zero* wherever the main plasma touches the wall [18]. Indeed, if this were not the case then it would be impossible for the halo current force to moderate the $n = 0$ and $n = 1$ instabilities, and so to convert them from modes growing on the Alfvén time to modes growing on the much longer L/R time of the vacuum vessel or the SOL plasma.

One effect which is absent from our model is the moderating influence of *eddy currents* flowing in that part of the vacuum vessel which is remote from the plasma once significant shrinkage of the plasma poloidal cross-section has taken place. On the other hand, eddy currents flowing in the part of the vacuum vessel that is either touching the plasma, or is in close proximity to it, are taken into account in the model. Generally speaking, we would expect the latter currents to play a more important role in VDEs than the former.

Finally, our model tacitly assumes that the inductive electric fields generated during a typical VDE are sufficiently large to cause the breakdown of any sheaths at the plasma/limiter boundary, and, consequently, that the halo current is not limited by the ion polarization current.

Acknowledgment

This research was funded by the US Department of Energy.

References

[1] Wesson J.A. 2004 *Tokamaks* 3rd edn (Oxford: Oxford University Press)
[2] Lazarus E.A., Lister J.B. and Neilson G.H. 1990 *Nucl. Fusion* **30** 111
[3] Walker M.L. and Humphreys D.A. 2009 *Automatica* **45** 665
[4] Gruber O., Lackner K., Paultasso G., Seidel U. and Streib B. 1993 *Plasma Phys. Control. Fusion* **35** B191
[5] Strait E.J., Lao L.L., Luxon J.J. and Reis E.E. 1991 *Nucl. Fusion* **31** 527
[6] Granetz R.S., Hutchinson I.H., Scorci J., Irby J.H., LaBombard B. and Gwinn D. 1996 *Nucl. Fusion* **36** 545
[7] Neyatani Y., Yoshino R., Nakamura Y. and Sakurai S. 1999 *Nucl. Fusion* **39** 559
[8] Knight P.J., Castle G.G., Morris A.W., Caloutsis A. and Gimblett C.G. 2000 *Nucl. Fusion* **40** 325
[9] Riccardo V., Hender T.C., Lomas P.J., Alper B., Bolzonella T., de Vries P., Maddison G.P. and JET EFDA Contributers 2004 *Plasma Phys. Control. Fusion* **46** 925
[10] Riccardo V. *et al* and JET EFDA Contributors 2009 *Nucl. Fusion* **49** 055012
[11] Caloutsis A. and Gimblett C.G. 1998 *Nucl. Fusion* **38** 1487
[12] Fitzpatrick R. 2008 *Phys. Plasmas* **15** 092502
[13] Humphreys D.A. and Kellman A.G. 1999 *Phys. Plasmas* **6** 2742
[14] ITER Physics Basis 1999 *Nucl. Fusion* **39** 2137
[15] Fitzpatrick R. 2009 *Phys. Plasmas* **16** 012506
[16] Freidberg J.P. and Haas F. 1973 *Phys. Fluids* **16** 1909
[17] Freidberg J.P. and Haas F. 1974 *Phys. Fluids* **17** 440
[18] Zakharov L.E. 2008 *Phys. Plasmas* **15** 062507
[19] Pomphrey N., Bialek J.M. and Park W. 1998 *Nucl. Fusion* **38** 449
[20] Jhang H. 2008 *Phys. Plasmas* **15** 022501
[21] Paccagnella R., Cavinato M., Bolzonella T., Ortolani S., Pautasso G., Schneider W., Lukash V., Khayrutdinov R. and Strauss H.R. 2005 *Fusion Eng. Des.* **75–79** 589
[22] Paccagnella R., Strauss H.R. and Breslau J. 2009 *Nucl. Fusion* **49** 035003
[23] Strauss H.R., Paccagnella R. and Brelau J. 2010 *Phys. Plasmas* **17** 082505